

1 Chapter 1

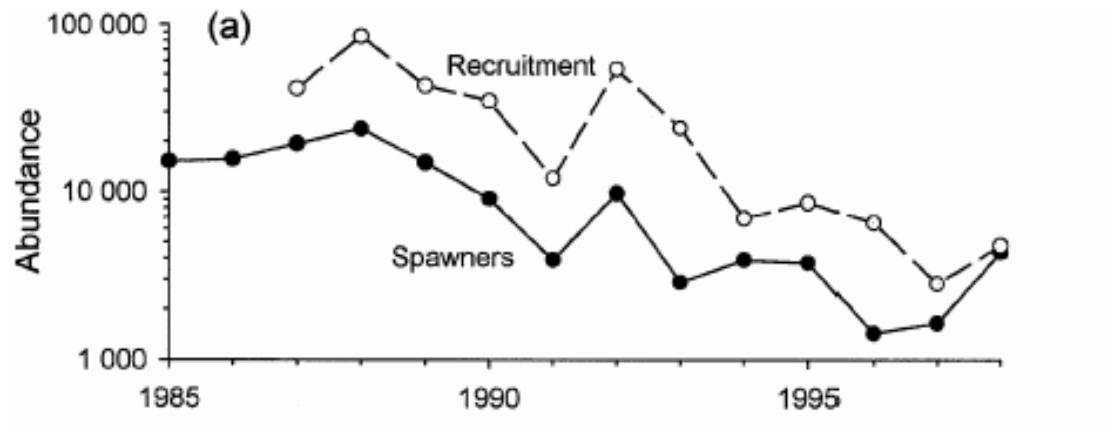


Figure 1.1: Decline in Coho salmon stocks on the Thomson River, BC (from Bradford and Irvine 2000)

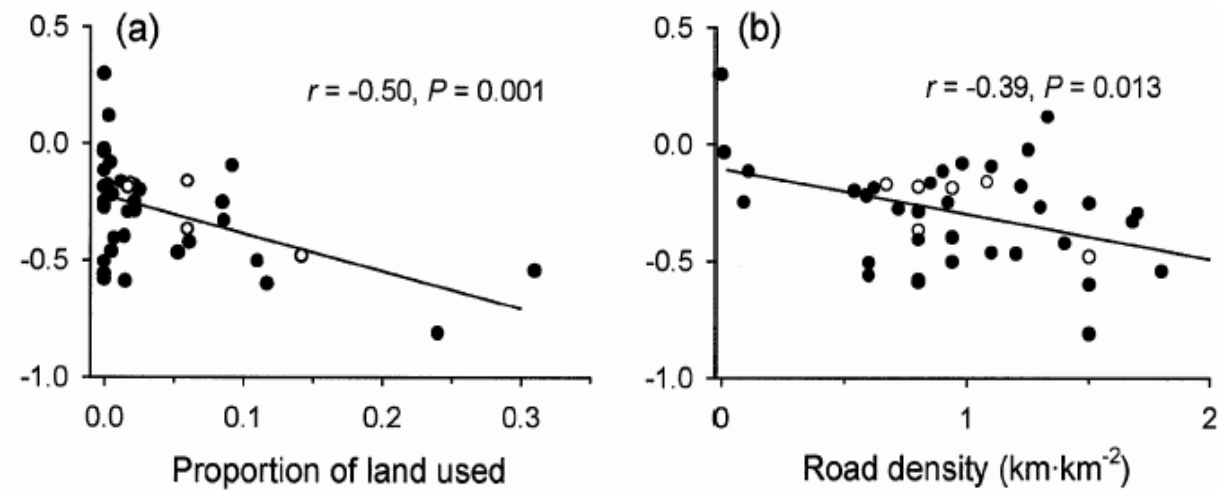


Figure 1.2: Rate of decline on individual streams is related to habitat variables; from Bradford and Irvine (2000).

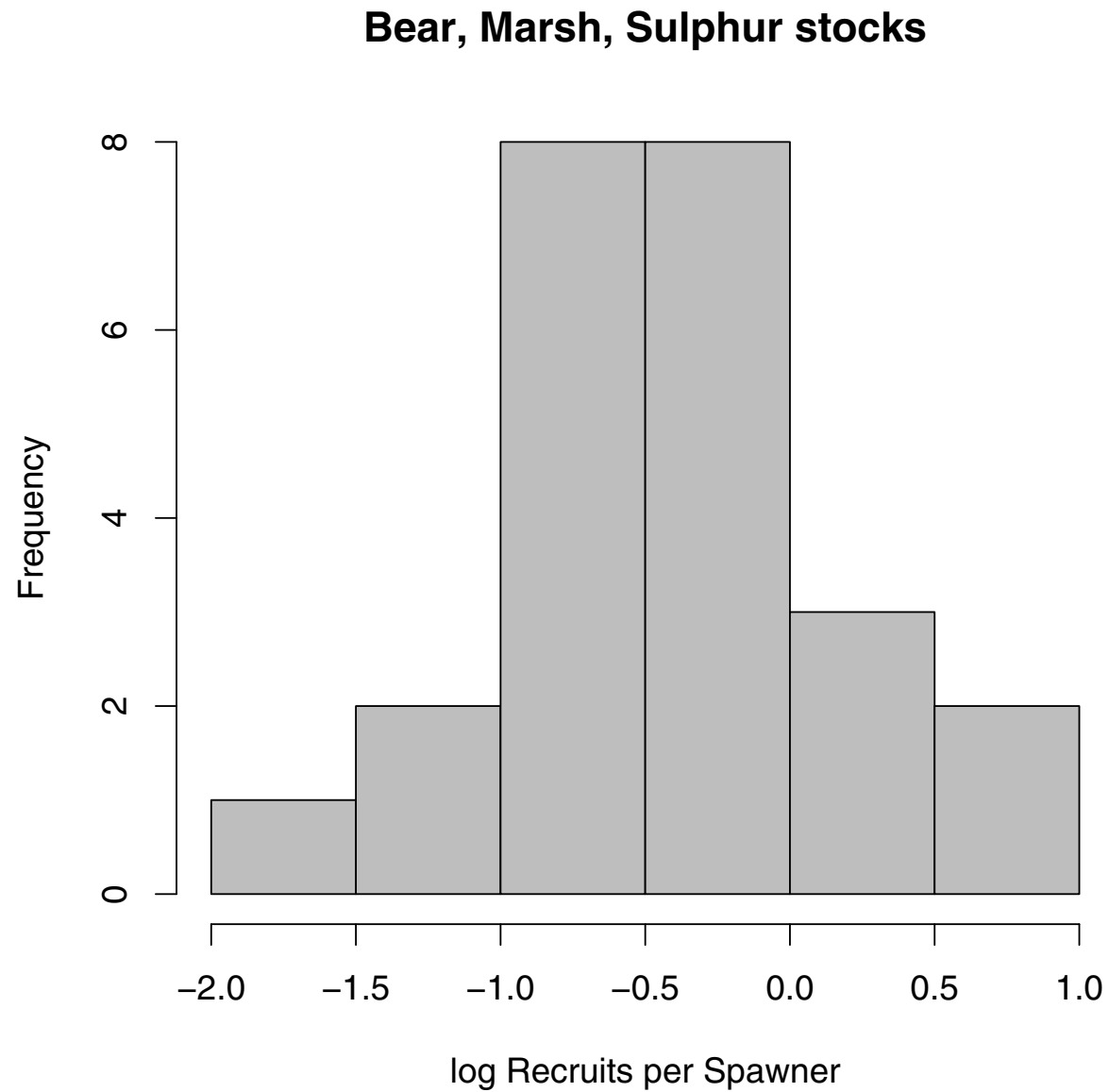


Figure 1.3: Frequency distribution of $\ln(\text{recruits per spawner})$ for the Bear, Marsh, and Sulphur Creek stocks of spring/summer run Chinook salmon, in “good” years.

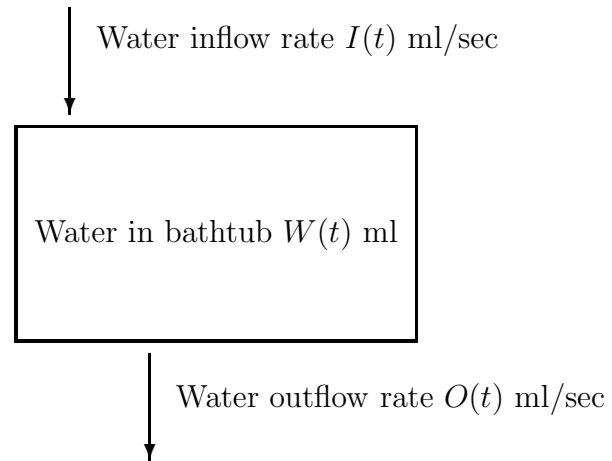


Figure 1.4: Compartment diagram of the bathtub model. The rectangle denotes the state variable – the amount of water in the tub – and the arrows denote flows.

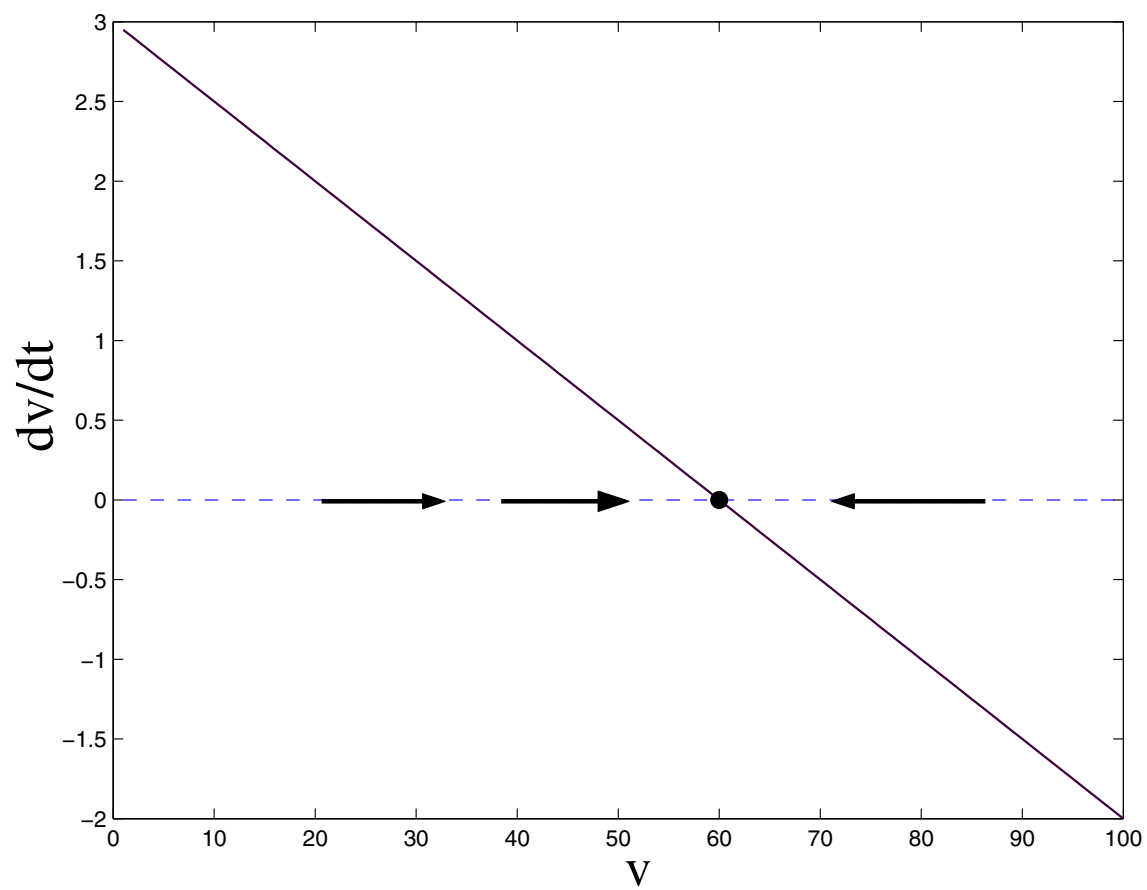


Figure 1.5: Graphical analysis of $dv/dt = k_1s - (k_{-1} + k_2 + k_1s)v$

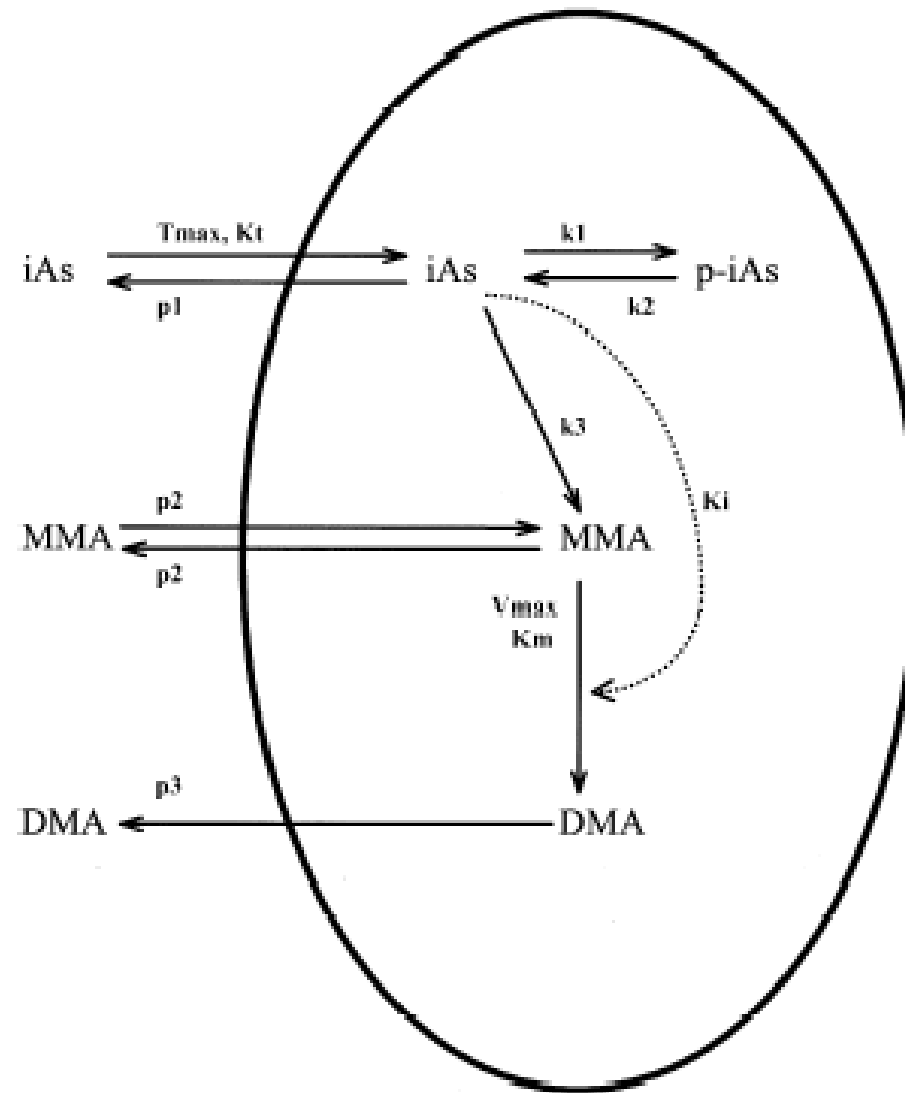


Figure 1.6: Compartment model for arsenic in rat hepatocytes, from Easterling et al. (2002).

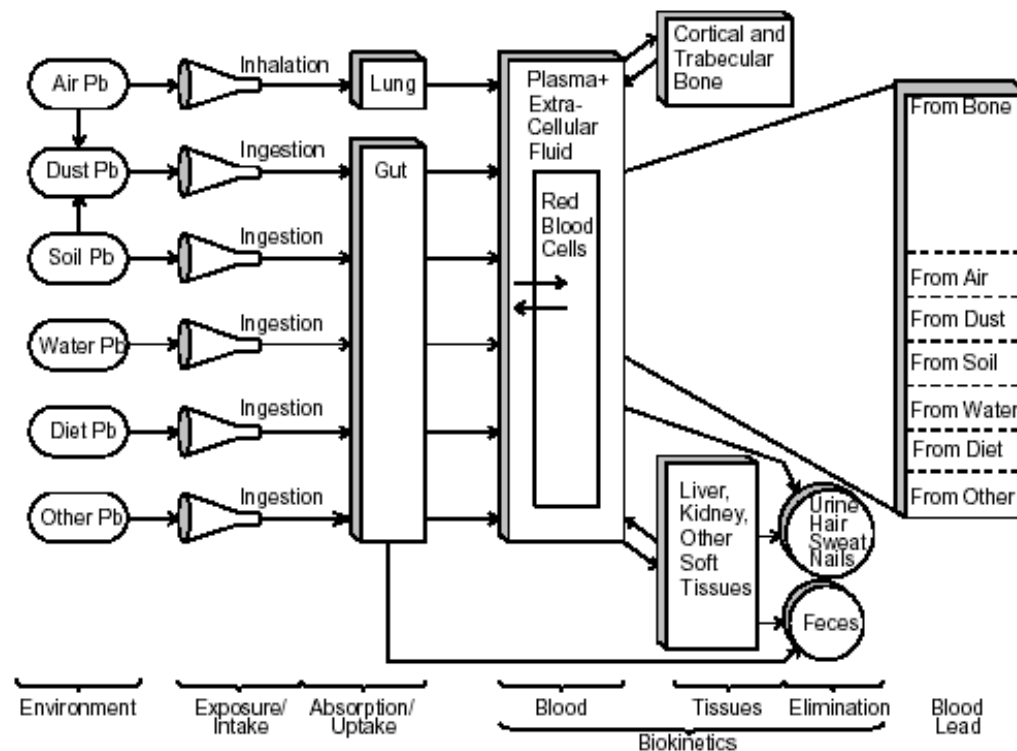


Figure 1.7: Compartment diagram for the IEUBK model for lead in children, from EPA (1994a). Ovals represent environmental levels of lead, rectangles are model compartments (forms of lead in the body that are distinguished in the model), and circles are losses of lead from the body.

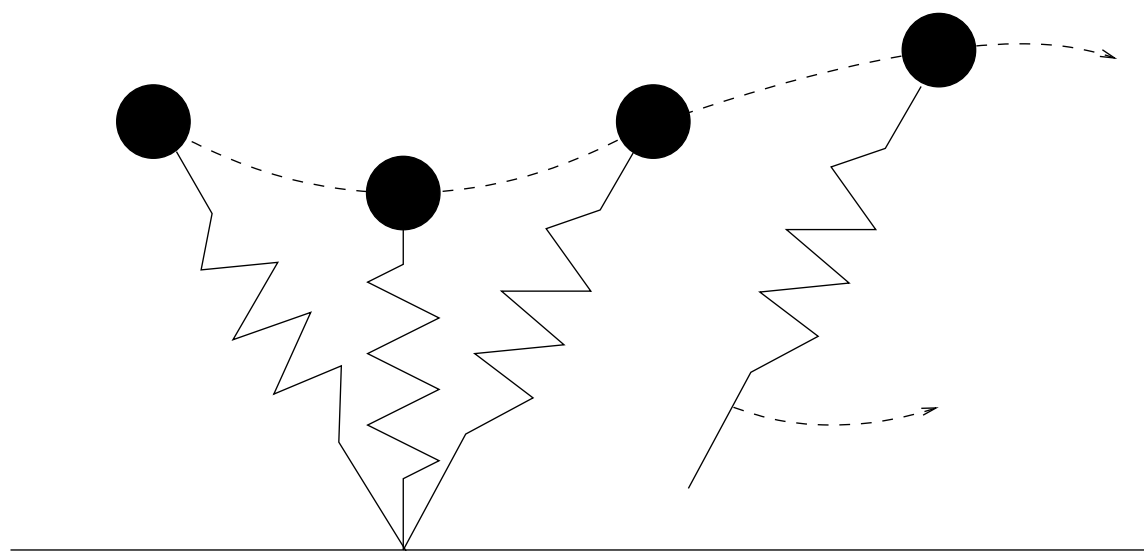


Figure 1.8: A cartoon of the pogo stick or monopode.

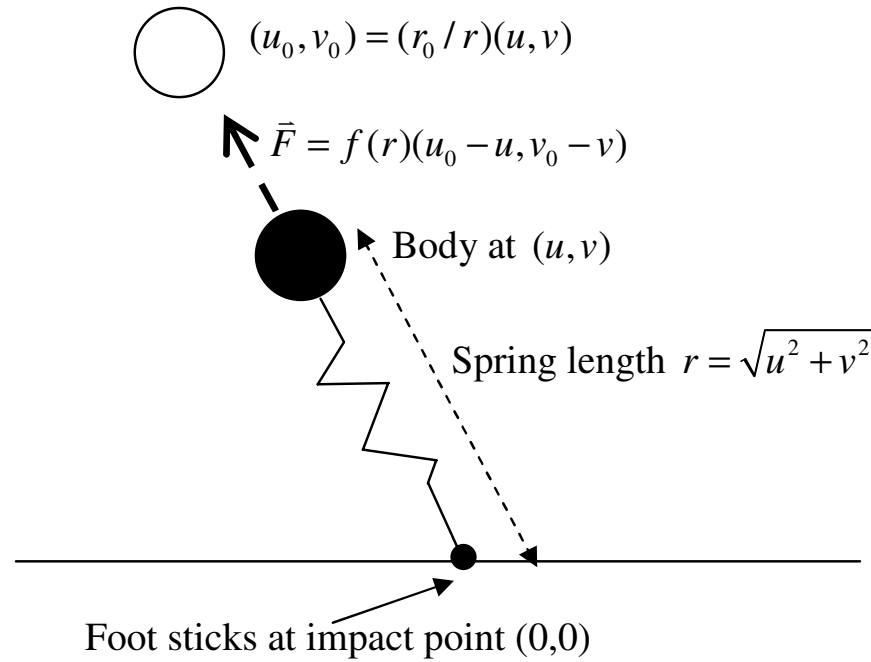


Figure 1.9: The monopod in stance phase. The dynamic equations are written in coordinates (u, v) giving the position of the body relative to the point where the foot meets the ground. The open circle shows the body's “resting position” corresponding to the leg at resting length r_0 , and the bold dashed arrow indicates the resulting force vector generated by the spring.

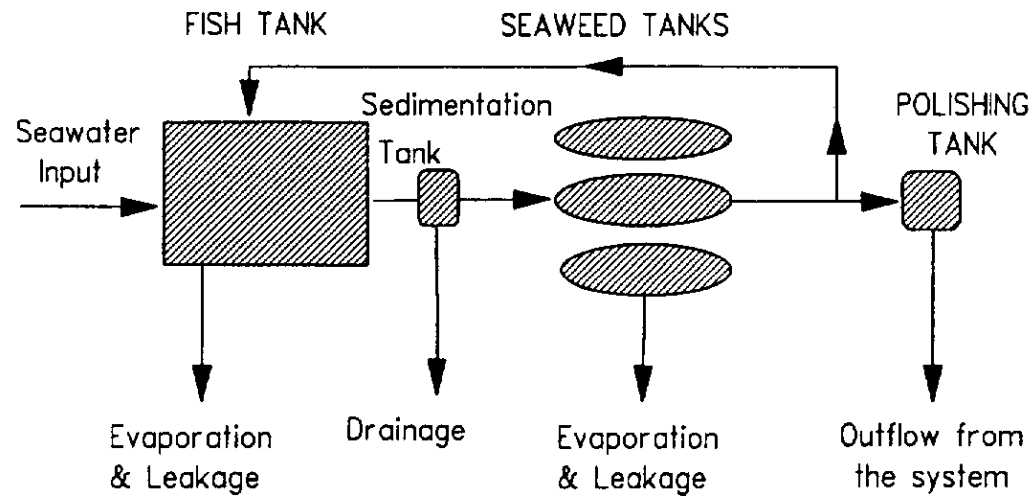


Figure 1.10: Diagram of the experimental fishpond system showing water flows between compartments.

Practical models	Theoretical models
Main goals are management, design, and prediction.	Main goals are theoretical understanding and theory development.
Numerical accuracy is desirable, even at the expense of simplicity.	Numerical accuracy is not essential; the model should be as simple as possible.
Processes and details can be ignored only if they are numerically unimportant.	Processes and details can be ignored if they are conceptually irrelevant to the theoretical issues.
Assumptions are quantitative representations of system processes.	Assumptions may be qualitative representations of hypotheses about the system, adopted conditionally in order to work out their consequences.
System- and question-specific.	Applies to a range of similar systems.

Table 1: Classification of models by objectives

2 Chapter 2

Category	Carapace length (mm)	Category	Plant area (cm ²)
Yearling		Seedling	0.5 - 5
Juvenile 1	<60	Juvenile	5.1 - 35
Juvenile 2	60-99	Adult 1*	35.1-200
Immature 1	100-139	Adult 2*	200.1-600
Immature 2	140-179	Adult 3*	> 600
Subadult*	180-207		
Adult 1*	208-239		
Adult 2*	>240		

Table 2: Two examples of stage classifications based in part on individual size. Asterisks indicate reproductive categories. The two left columns give the categories used by Doak et al. (1994) for desert tortoise in the western Mojave desert, which were the same as those used by the Bureau of Land Management in the population monitoring program that provided the data for the model. The two right columns give the categories defined by Valverde and Silvertown for the forest herb *Primula vulgaris*.

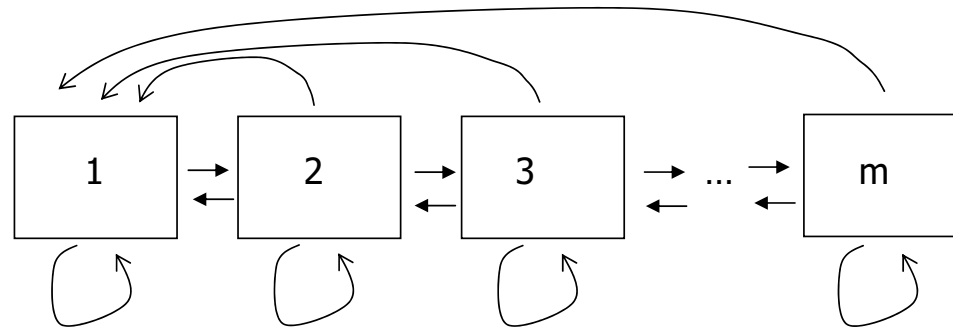


Figure 2.1: The standard size-class model. Size categories are broad enough that individuals can't change by more than one category between population censuses, and all newborn individuals are in the smallest size class. These all look the same apart from the number of “stages”.

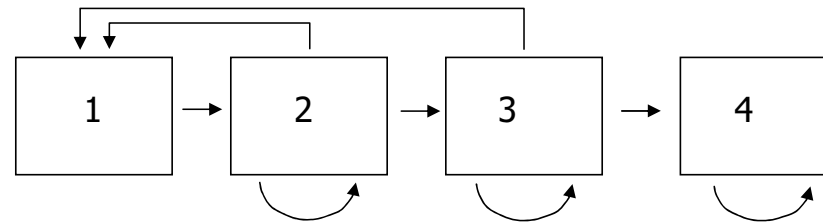


Figure 2.2: Stage-structured model for killer whales (Brault and Caswell 1993). The stages recognized were 1=Yearling, 2=Juvenile, 3=Mature female, and 4=Post-reproductive female.

Model	$\mathbf{n}(t+1) = \mathbf{A}\mathbf{n}(t), \mathbf{n}(0) = \mathbf{n}_0$
Solution	$\mathbf{n}(t) = \mathbf{A}^t \mathbf{n}_0$
Eigenmode Expansion	$\mathbf{n}(t) = \sum c_i \lambda_i^t \mathbf{w}_i$
Long-term exponential growth	$\sum_i n_i(t) \sim c \lambda^t$ as $t \rightarrow \infty$
Stable Stage Distribution	$\mathbf{n}(t) \sim c \lambda^t \mathbf{w}$
Stage-specific reproductive value	Proportional to \mathbf{v}
Eigenvalue sensitivity formula	$\frac{\partial \lambda}{\partial a_{ij}} = \frac{v_i w_j}{\mathbf{v} \cdot \mathbf{w}}$

Table 3: Main properties of a matrix model with power-positive projection matrix \mathbf{A} .

$$\mathbf{A} = \begin{bmatrix} 0 & 0 & 0 & 0 & 0 & f_6 & f_7 & f_8 \\ .716 & .567 & 0 & 0 & 0 & 0 & 0 & 0 \\ 0 & .149 & .567 & 0 & 0 & 0 & 0 & 0 \\ 0 & 0 & .149 & .604 & 0 & 0 & 0 & 0 \\ 0 & 0 & 0 & .235 & .560 & 0 & 0 & 0 \\ 0 & 0 & 0 & 0 & .225 & .678 & 0 & 0 \\ 0 & 0 & 0 & 0 & 0 & .249 & .851 & 0 \\ 0 & 0 & 0 & 0 & 0 & 0 & .016 & .860 \end{bmatrix} \quad (2.1)$$

$$(f_6, f_7, f_8) = [0.042, 0.069, 0.069]$$

$$\text{or } [0.42, 0.69, 0.69]$$

$$\text{or } [1.30, 1.98, 2.57]$$

$$\text{or } [2.22, 3.38, 4.38].$$

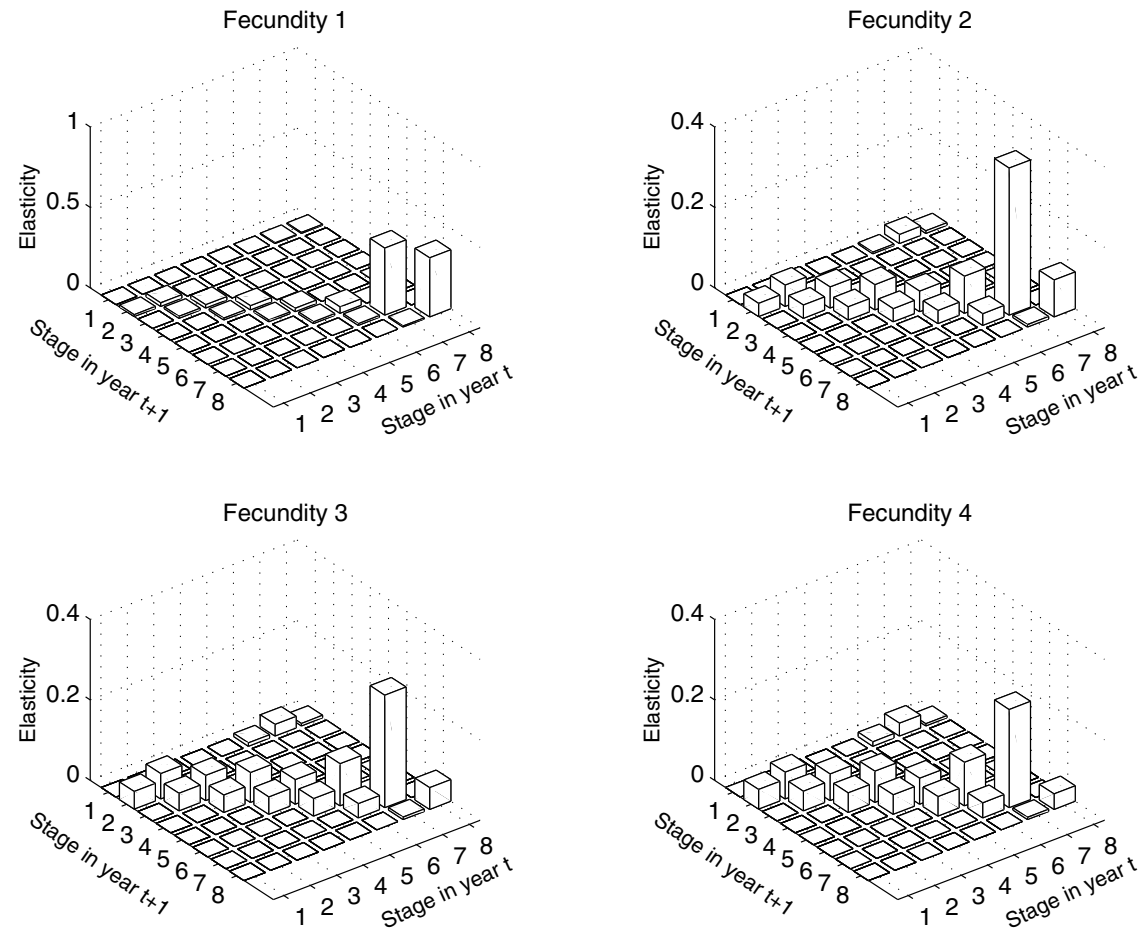


Figure 2.3: Eigenvalue elasticities for the Doak et al. (1994) stage-structured model for desert tortoise. The stages are 1=yearling, 2,3=juveniles, 4,5=immature, 6=subadult, 7=smaller adult, 8=larger adult.

$$\mathbf{A} = \begin{bmatrix} 0 & 0 & 0 & 4.665 & 61.896 \\ 0.675 & 0.703 & 0 & 0 & 0 \\ 0 & 0.047 & 0.657 & 0 & 0 \\ 0 & 0 & 0.019 & 0.682 & 0 \\ 0 & 0 & 0 & 0.061 & 0.8091 \end{bmatrix}$$

$\sigma_i =$ survival probability

$\gamma_i =$ growth probability, conditional on survival

On diagonal: $P_i = \sigma_i(1 - \gamma_i)$ survive & remain in stage

Sub-diagonal: $G_i = \sigma_i\gamma_i$ survive & grow to next stage



Figure 2.4: Eigenvalue elasticities for the Crowder et al. (1994) stage-structured model for Loggerhead sea turtles. Stages [stage durations] in the model are 1=egg and hatchling[1 yr], 2=small juvenile[7 yr], 3=large juvenile[8 yr], 4=subadult[6 yr], 5=adult[indefinite].

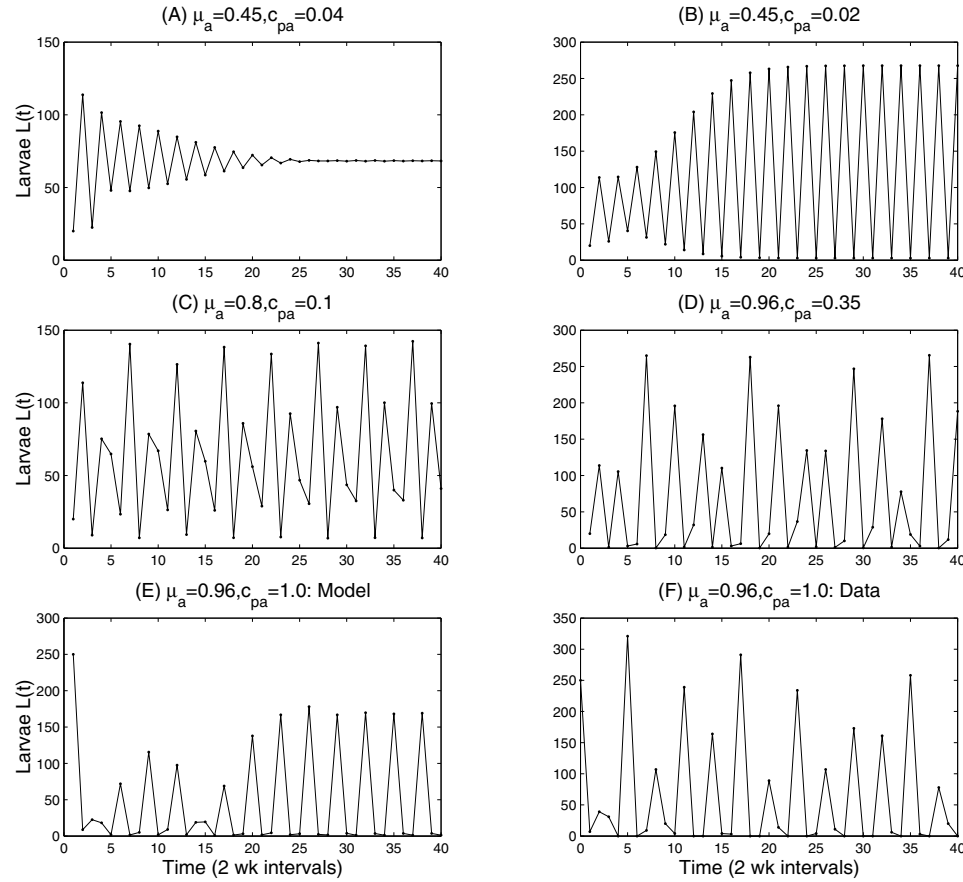


Figure 2.5: The LPA model. Panels (A)-(D) show simulations started with 20 individuals in each life stage and running for 40 two-week time steps of the model. Panels (E) and (F) compare model simulations with experimental results for high values of μ_a and c_{pa} ; model simulations used the same initial conditions as the experiments, $[L(0), P(0), A(0)] = [250, 5, 100]$.

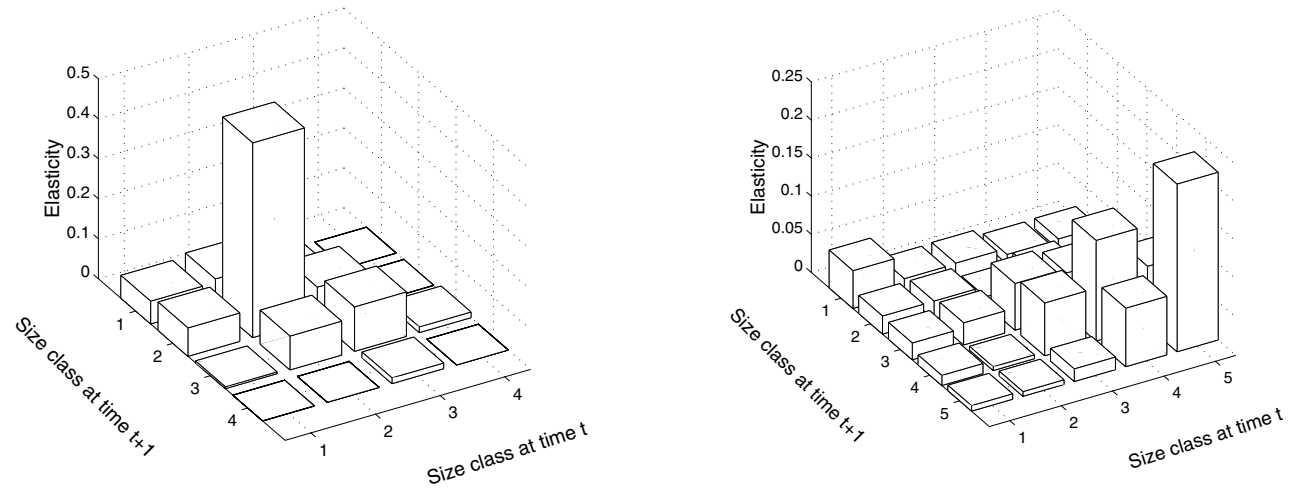


Figure 2.6: Left panel: Eigenvalue elasticities for a matrix model of Northern Monkshood using the size-based classification of Dixon and Cook: seedling, juvenile, small ($<2\text{mm}$), medium ($2\text{--}4\text{mm}$), and large ($>4\text{mm}$). The seedling stage is omitted because the subset of populations used to parameterize the model did not have any reproduction by seed during the study period. Right panel: Eigenvalue elasticities when class boundaries are set based on stem diameter, so that each class contained the same number of censused individuals.

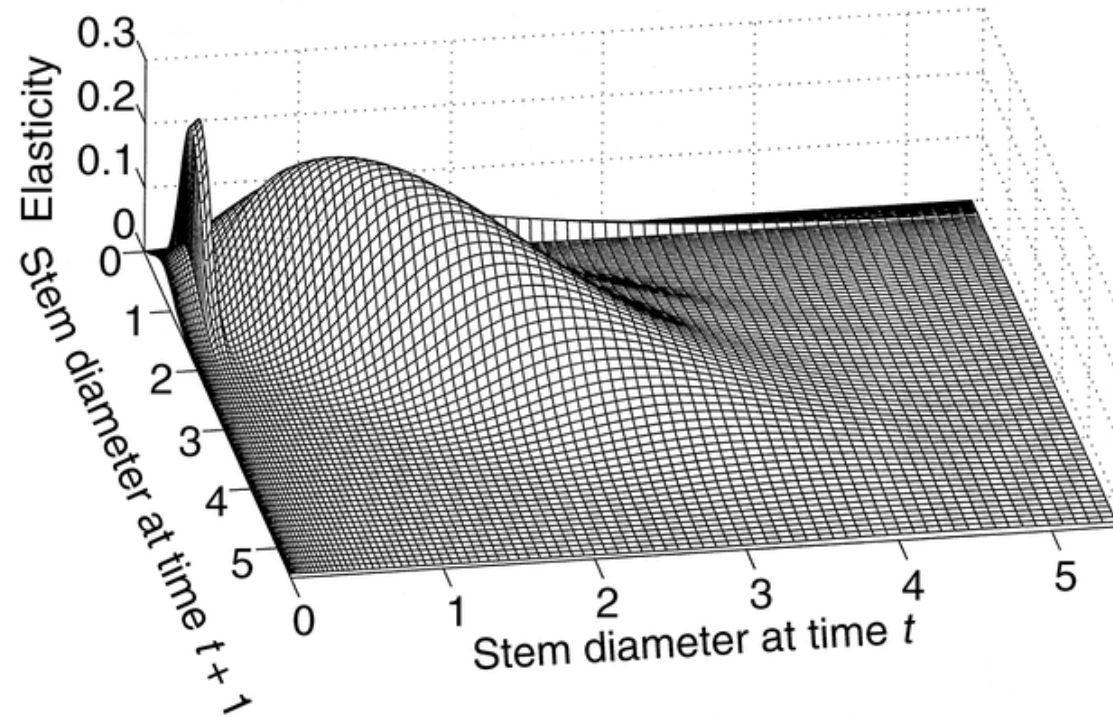


Figure 2.7: Elasticity surface for the integral projection model for Northern Monkshood.

3 Chapter 3

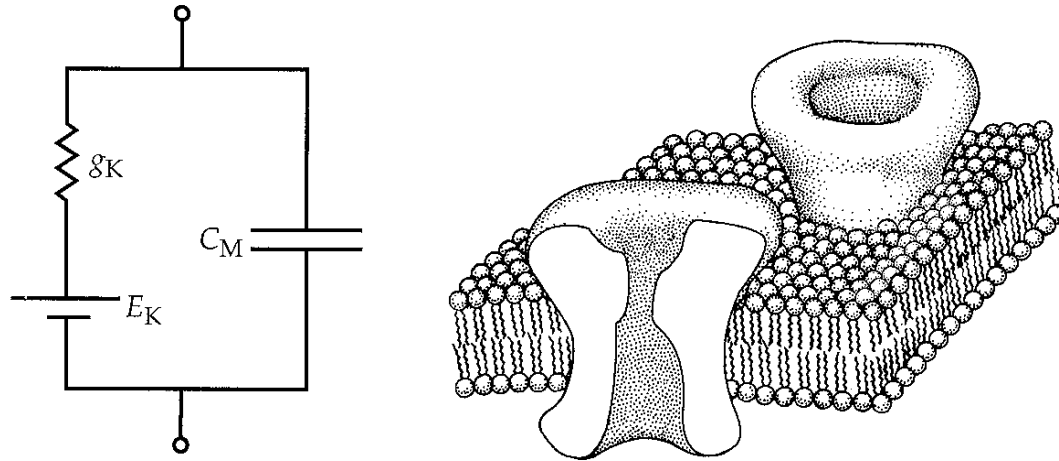


Figure 3.1: Artist's representation of a membrane spanning channel with a diagram representing an equivalent electrical circuit for the channel. From Hille(2001), p. 17

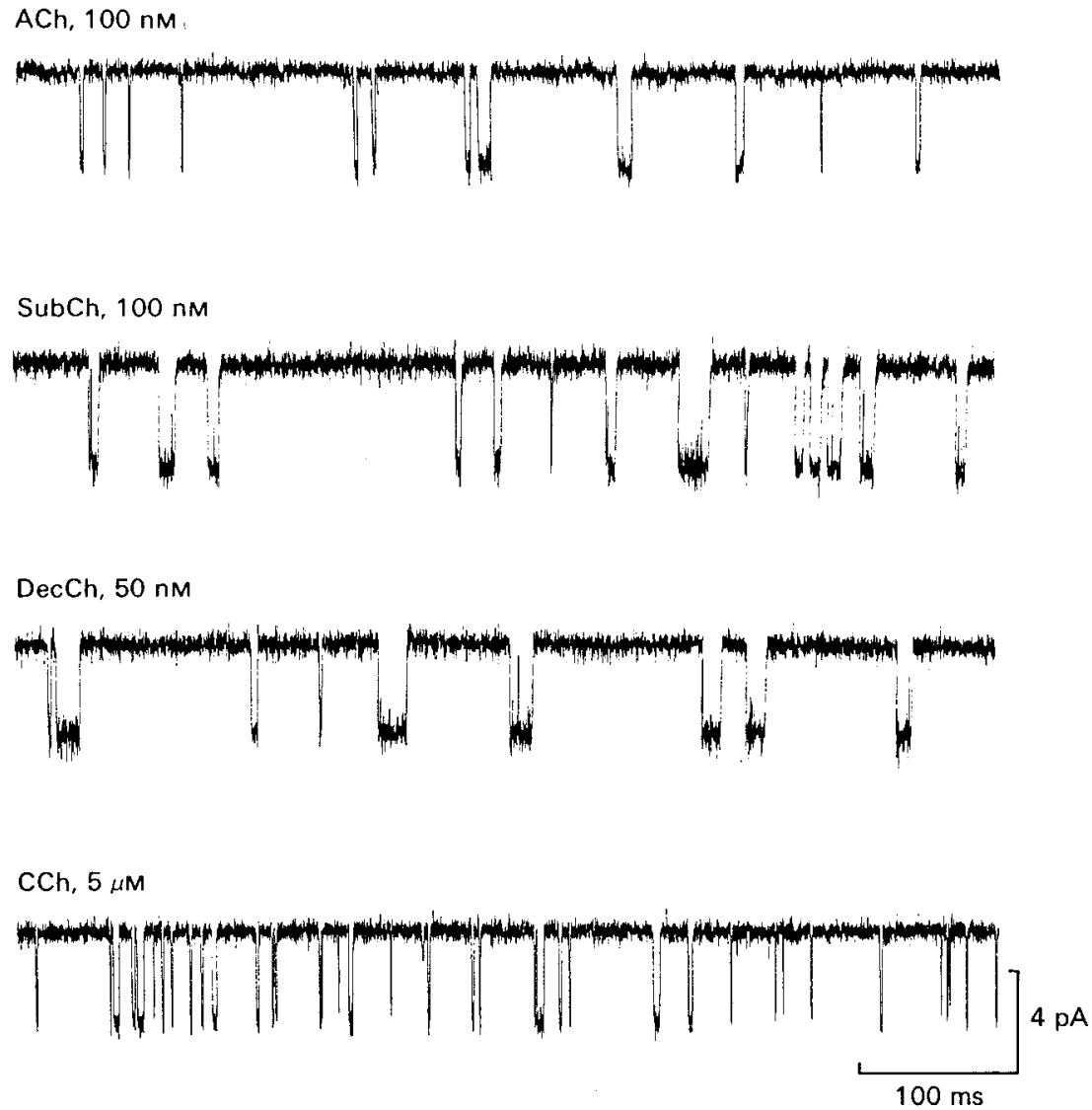


Figure 3.2: Data from a single channel recording of the nicotinic acetylcholine receptor (nAChR) channel in the neuromuscular junction, in the presence of four different agonists that can bind to the receptor. Note that the open channel current is the same for each agonist, but the dwell times are different. From Colquhoun and Sakmann (1985).

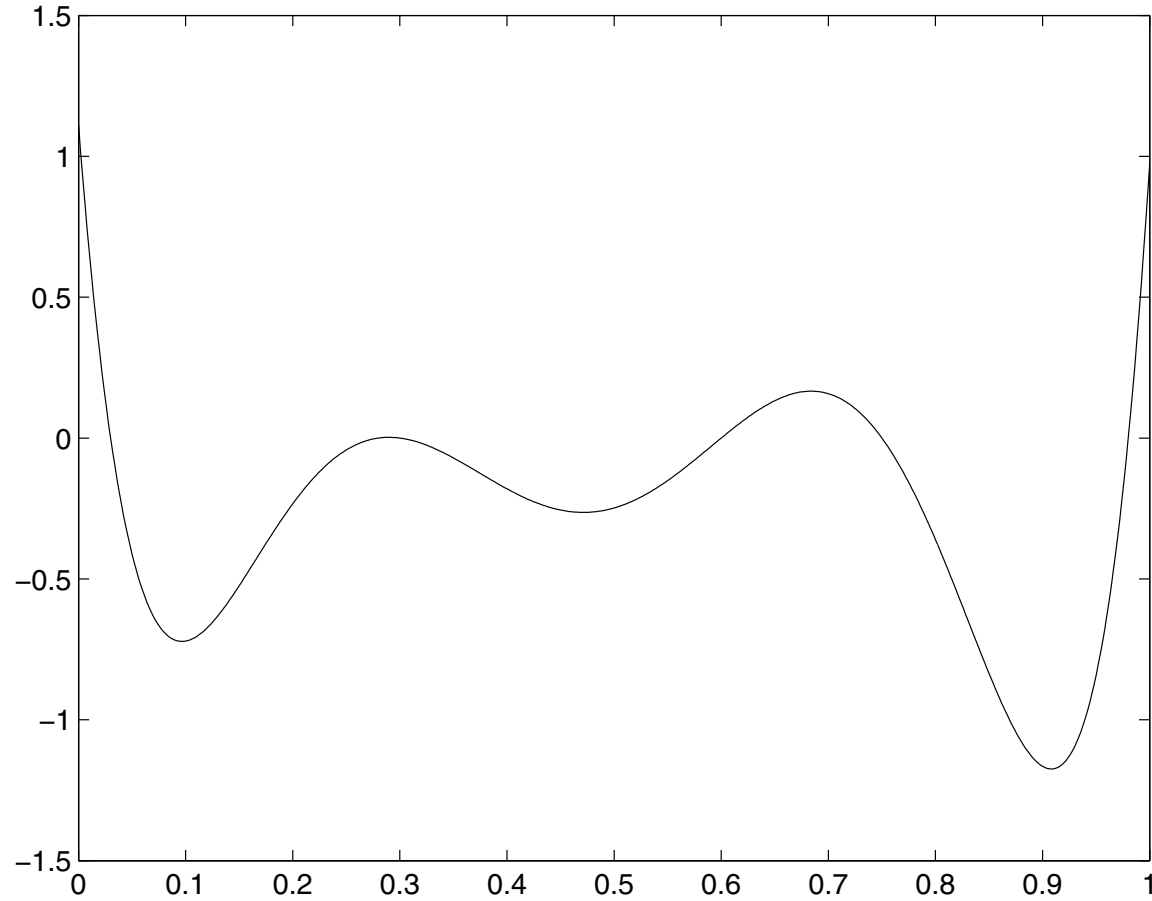


Figure 3.3: A hypothetical energy landscape. Imagine a ball rolling along this curve under the influence of gravity and collisions with other, much smaller particles. When the ball sits at a local minimum, it stays near this minimum until it receives a “kick” hard enough to knock it over one of the adjacent local maxima.

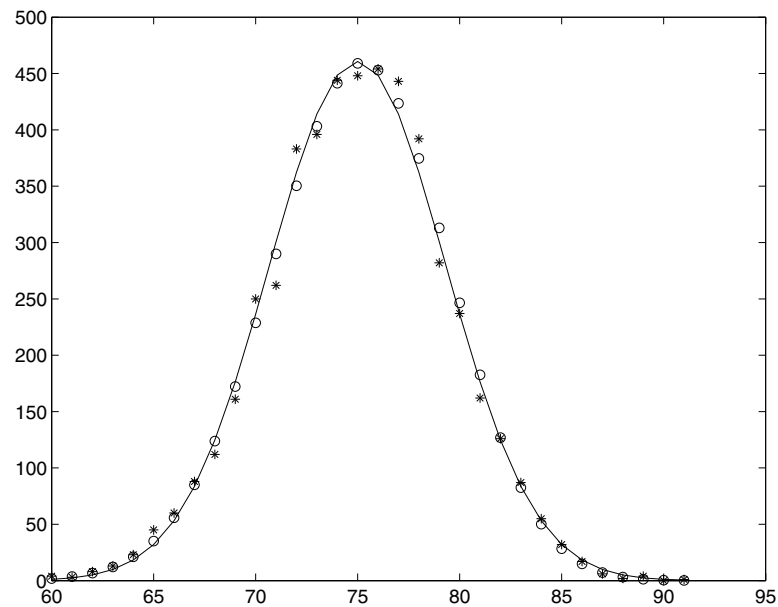


Figure 3.4: A histogram from a computer experiment: 5000 repetitions of tossing an unfair coin 100 times. The probability of heads is 0.75 and the probability of tails is 0.25. The asterisks show the number of experiments that produced k heads as a function of k , the circles are the values of the binomial distribution, and the solid line is the approximation to the binomial distribution from the bell shaped Gaussian function. Note that the minimal number of heads obtained in our trials was 60 and the maximum was 91. There are small deviations from the predicted distribution that change when we rerun the experiment with different sequences of the random numbers used to generate the experimental outcome.

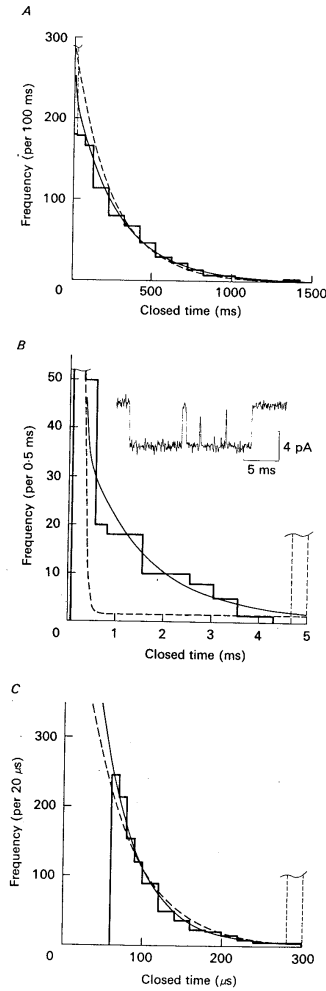


Figure 3.5: Sums of exponentials fit to dwell time distributions of open states in an nAChR channel. The three histograms show distributions of dwell times from three ranges of times: slow (top), medium (middle) and fast (bottom). The dashed curves come from a fit to a sum of two exponentials, the solid curves from a fit to a sum of three exponentials. From Colquhoun and Sakmann (1985).

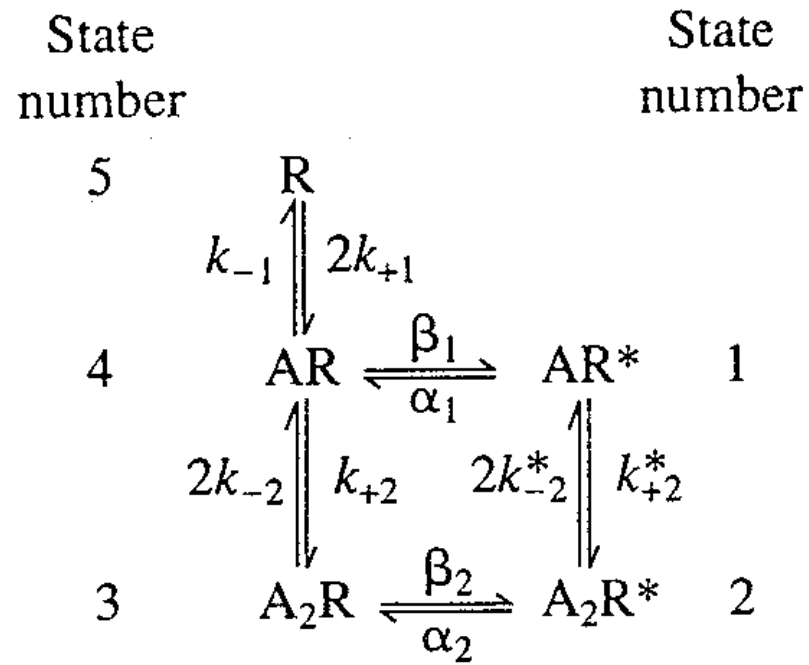


Figure 3.6: A diagram of the states and transitions in the Markov chain model used to model the nAChR channel From Colquhoun and Sakmann (1985). The states labeled with an * are the open states.

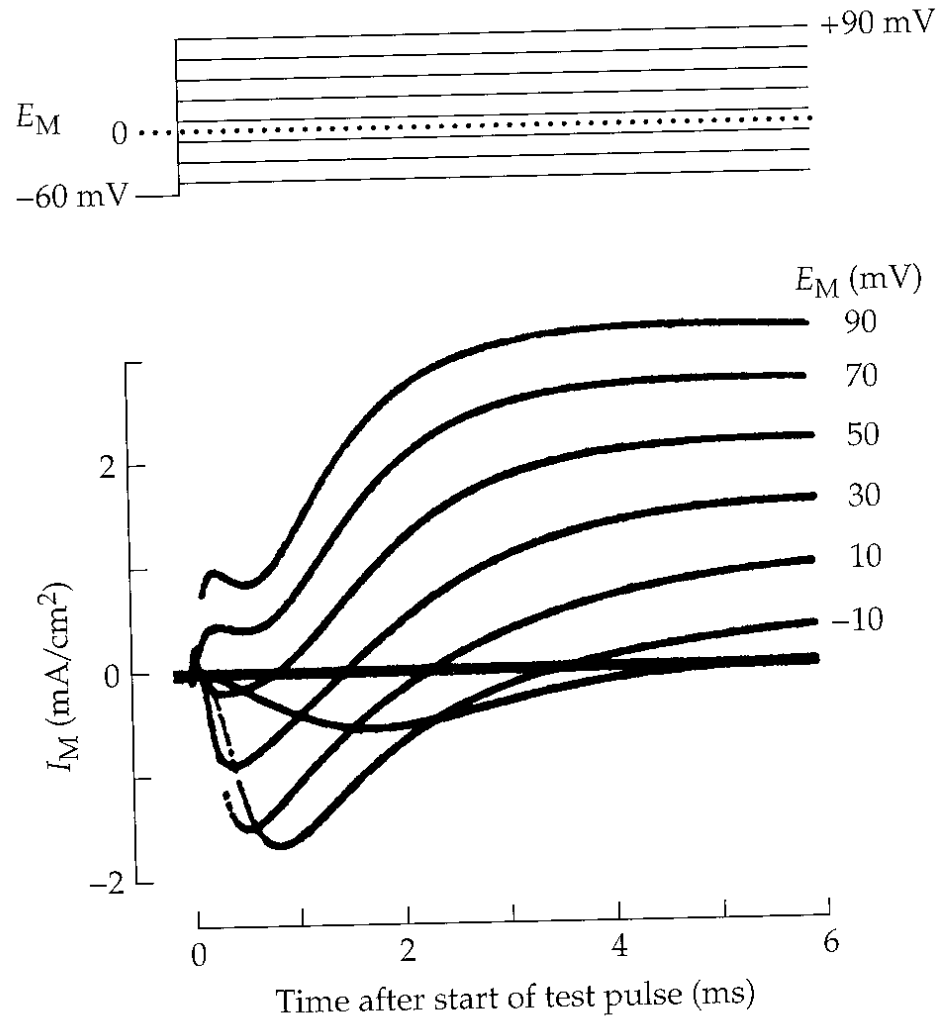


Figure 3.7: Data from a series of voltage clamp measurements on a squid giant axon. The membrane is held at a potential of -60mV and then stepped to higher potentials. The traces show the current that flows in response to the voltage steps. From Hille(2001), p.38.

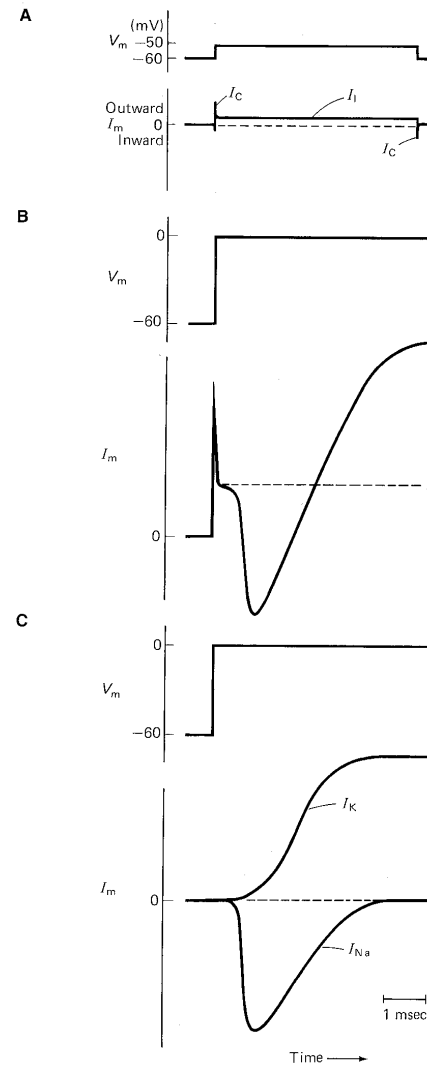


Figure 3.8: The separation of voltage clamp currents in the squid axon into sodium and potassium currents. Pharmacological blockers (TTX for sodium, TEA for potassium) are used to block channels and remove the contribution of the blocked channels from the voltage clamp current. The spikes at the beginning of the step in the second and fourth traces and at the end of the second trace is capacitive current due to the redistribution of ions on the two sides of the membrane when its potential changes. From Kandel et al. (1991), p.107.

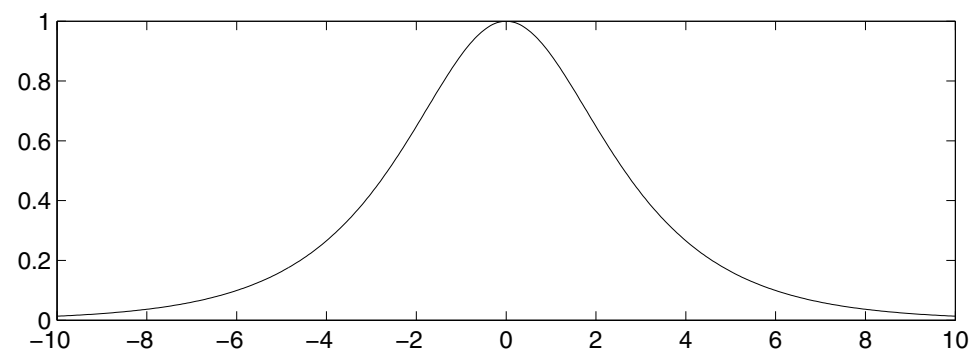
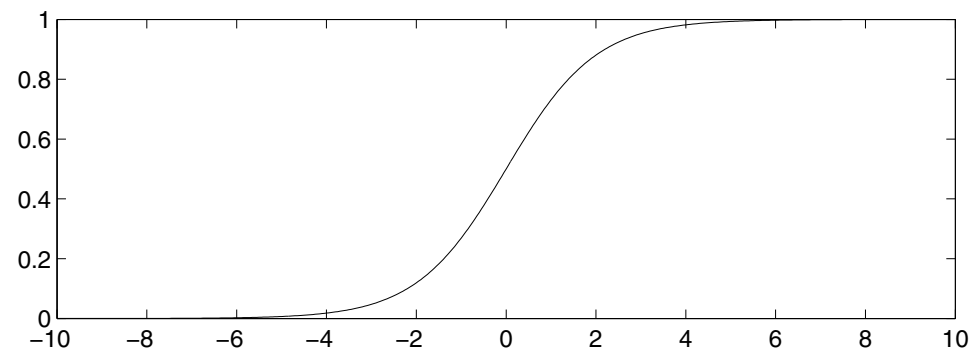


Figure 3.9: Plots of the functions $\frac{1}{1+\exp(-v)}$ and $\frac{1}{\cosh(\frac{v}{2})}$

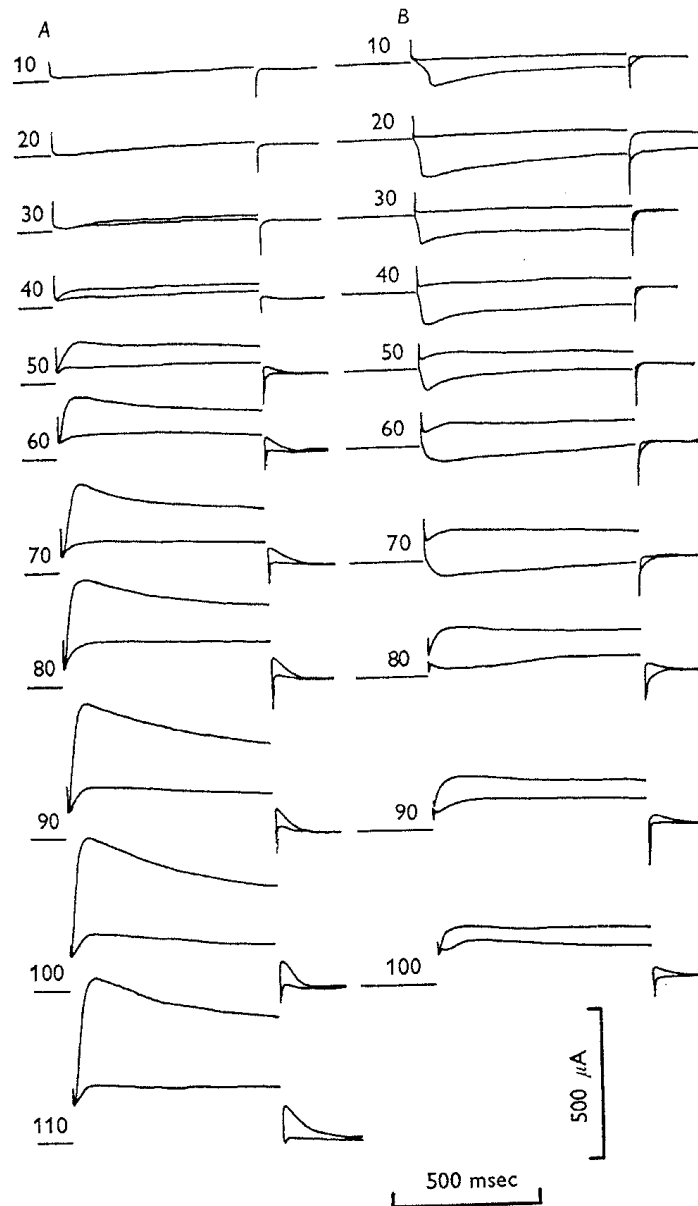


Figure 3.10: Voltage clamp currents in a barnacle muscle fiber. The left hand column shows currents elicited in a Ca^{2+} free bathing medium, thereby eliminating calcium currents. The right hand column shows currents elicited in a muscle fiber perfused with TEA to block potassium currents. Note that the currents that follow the depolarizing voltage step are shown as well as those during the step. From Keynes et al.(1973), figure 8.

4 Chapter 4

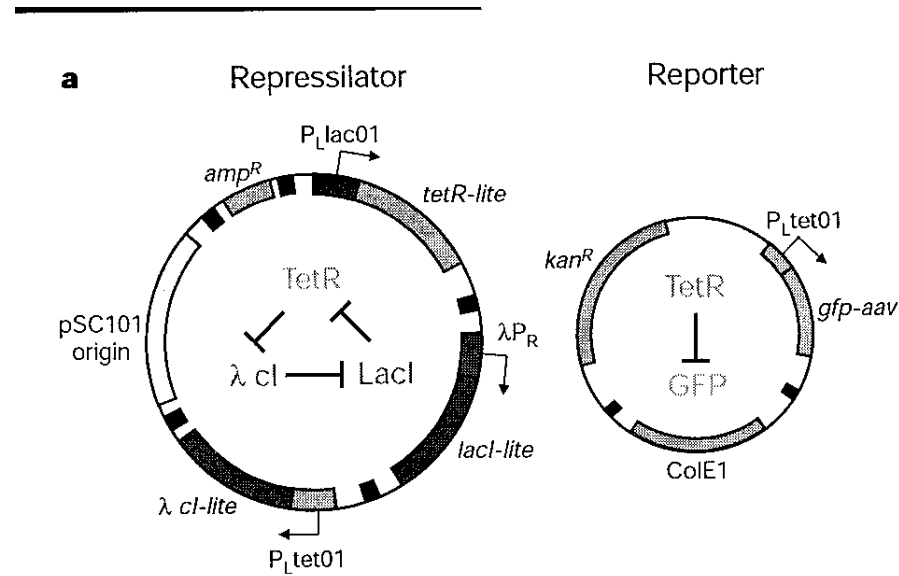


Figure 4.1: A schematic diagram of the repressilator. Genes for the *lacI*, *TetR* and *cl* repressor proteins together with their promoters are assembled on a plasmid which is inserted into an *E. coli* bacterium. A second plasmid that contains a *TetR* promoter region and a gene that codes for green fluorescent protein is also inserted into the bacterium. In the absence of *TetR*, the bacteria with these plasmids will produce green fluorescent protein. From Elowitz and Leibler (2000)

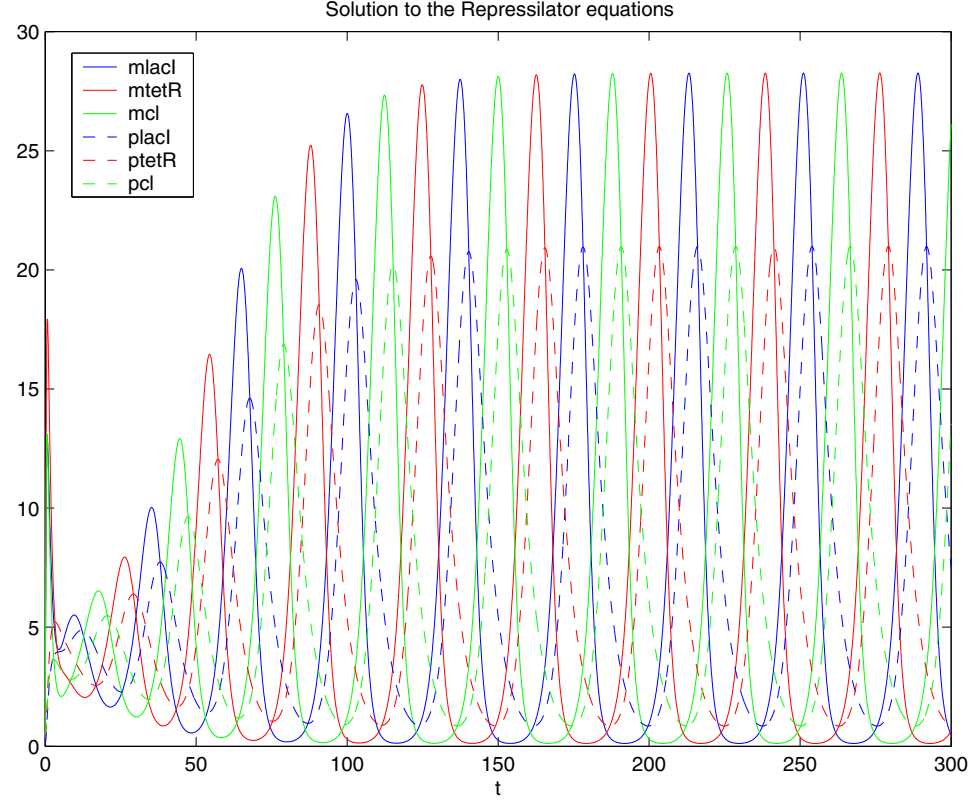


Figure 4.2: Solutions of the repressilator equations with initial conditions $(m_{lacI}, m_{tetR}, m_{cl}, m_{lacI}, m_{tetR}, m_{cl}) = (0.2, 0.1, 0.3, 0.1, 0.4, 0.5)$ and parameters $(\alpha_0, \alpha, \beta, n) = (0, 50, 0.2, 2)$.

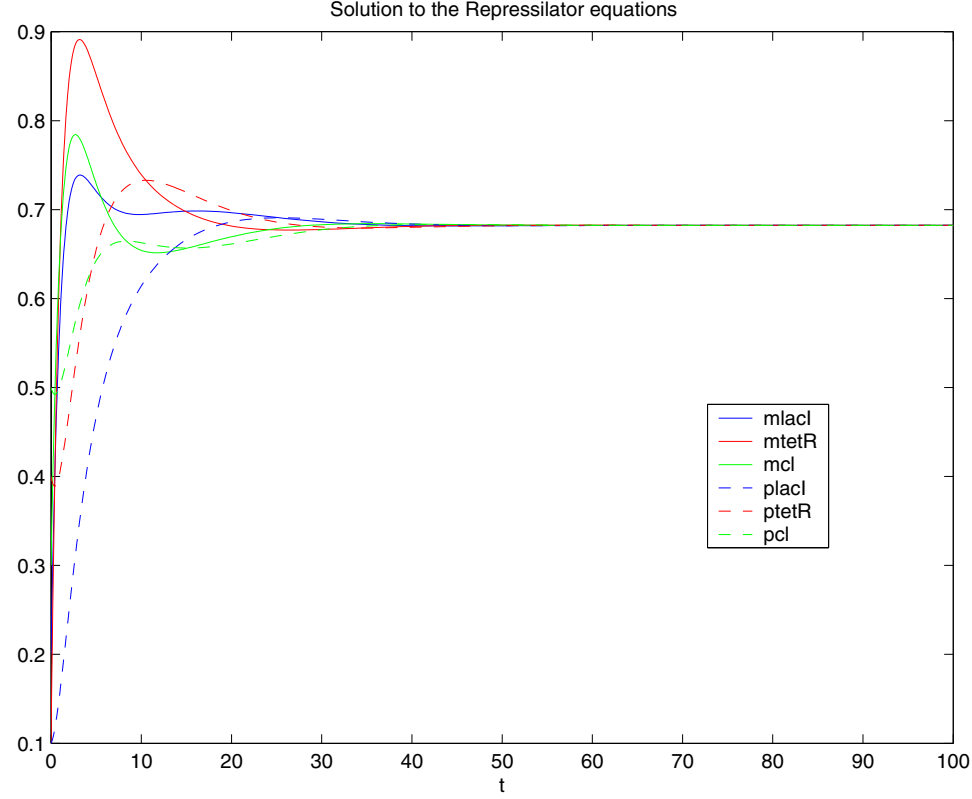


Figure 4.3: Solutions of the repressilator equations with initial conditions $(m_{lacI}, m_{tetR}, m_{cl}, m_{lacI}, m_{tetR}, m_{cl}) = (0.2, 0.1, 0.3, 0.1, 0.4, 0.5)$ and parameters $(\alpha_0, \alpha, \beta, n) = (0, 1, 0.2, 2)$.

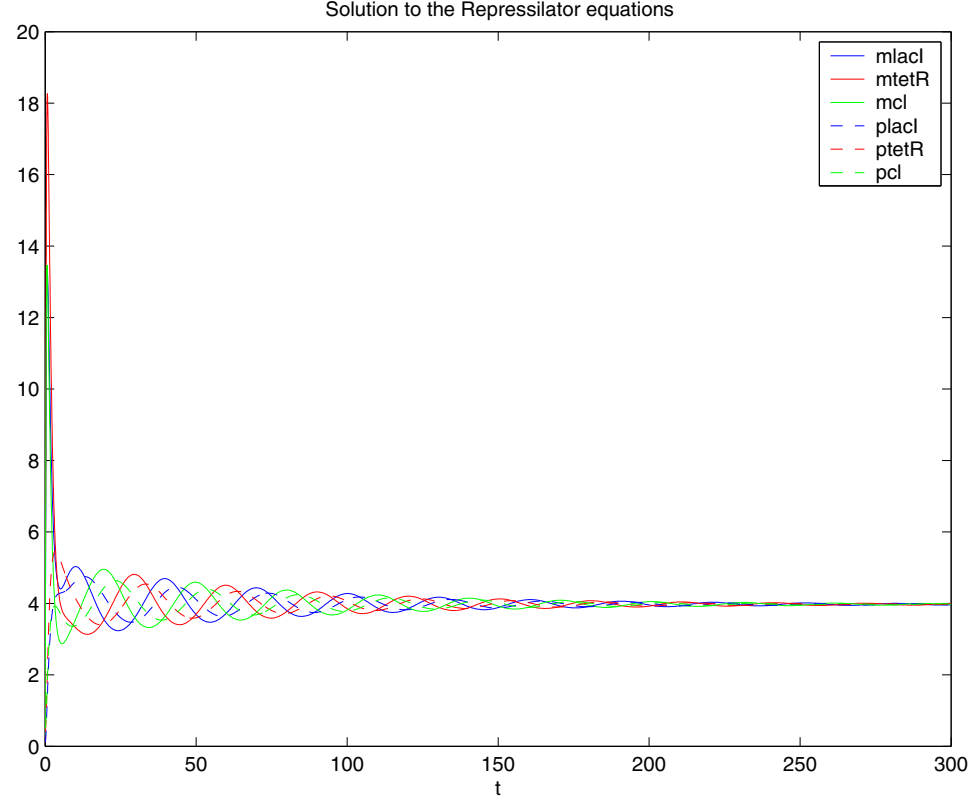


Figure 4.4: Solutions of the repressilator equations with initial conditions $(m_{lacI}, m_{tetR}, m_{cl}, m_{lacI}, m_{tetR}, m_{cl}) = (0.2, 0.1, 0.3, 0.1, 0.4, 0.5)$ and parameters $(\alpha_0, \alpha, \beta, n) = (1, 50, 0.2, 2)$.

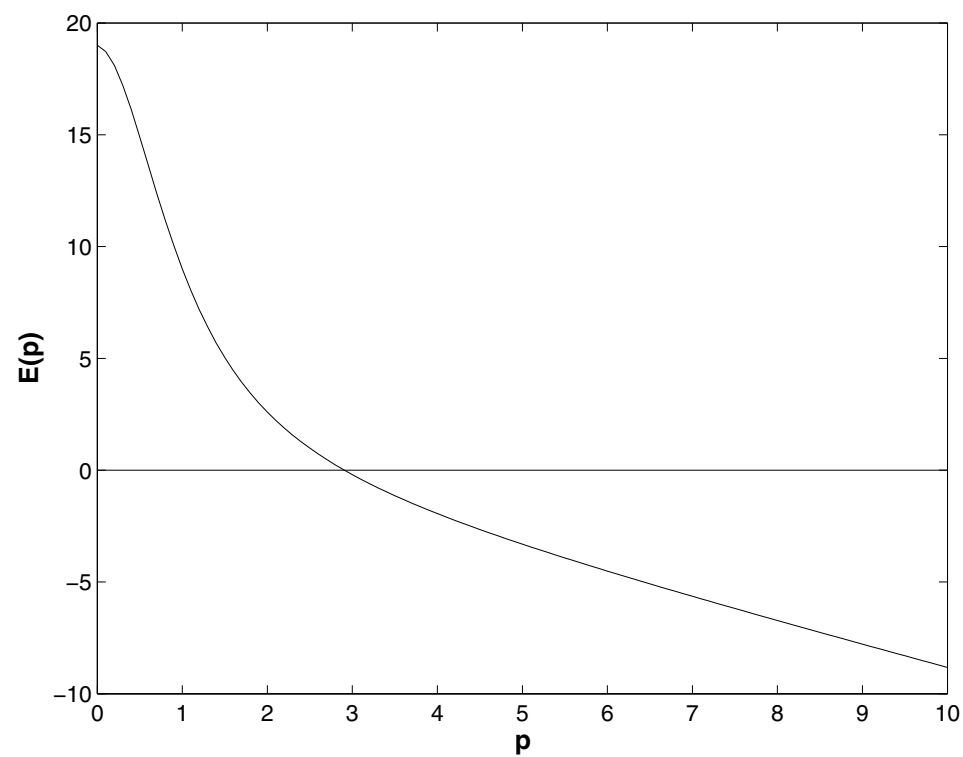


Figure 4.5: Graph of the function $E(p) = -p + \frac{18}{1+p^2} + 1$

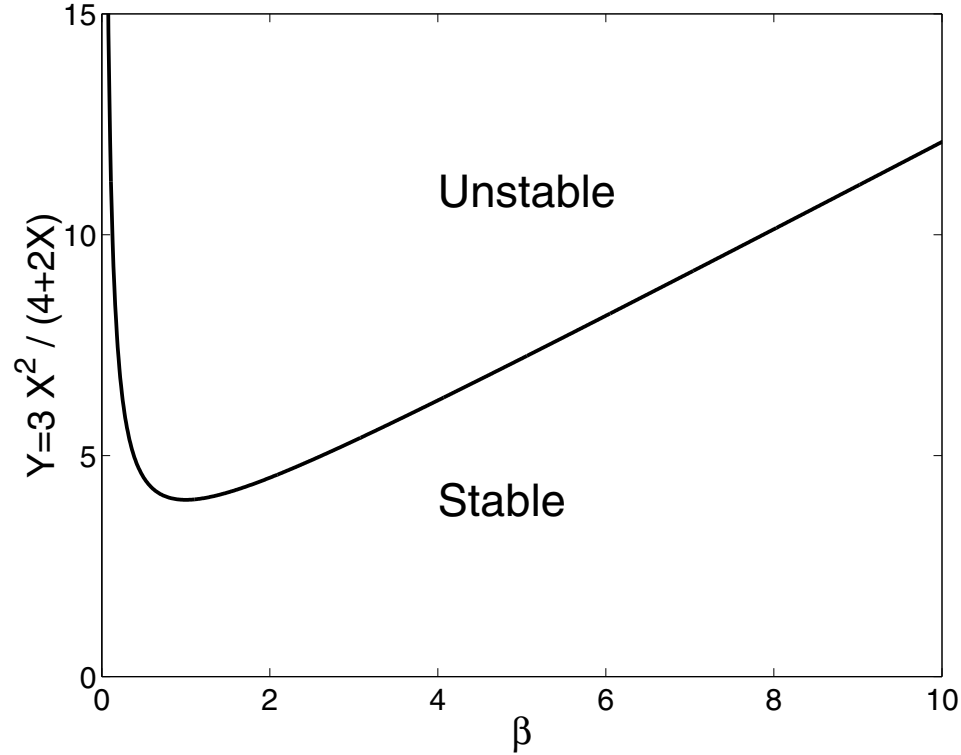


Figure 4.6: Diagram of the stability region for the repressilator system in terms of β and the parameter combination $Y = 3X^2/(4 + 2X)$. Note: the system is also unstable for $X < -2$ (i.e. $Y < 0$), which cannot occur for cooperativity parameter $n = 2$ but is possible for larger n .

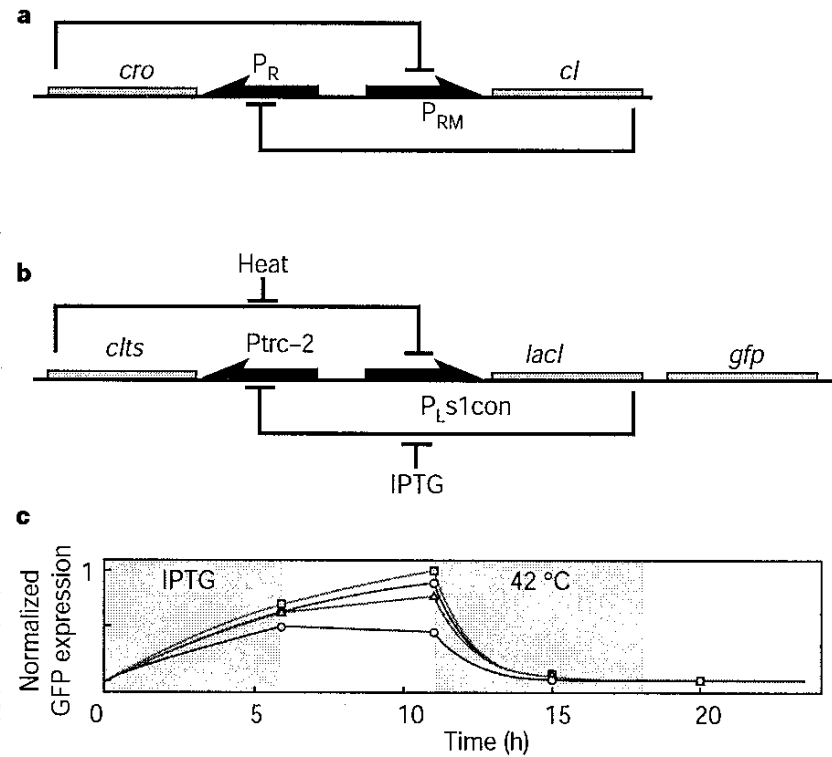


Figure 4.7: A schematic diagram of bistable gene regulatory networks in bacteriophage λ . Two genes code for repressor proteins of the other gene. (a) A natural switch. (b) A switch engineered from *cl* and *lacI* genes in which the repressor of the *lacI* gene is a temperature sensitive version of the *Cl* protein. Green fluorescent protein is also produced when the *cl* gene is expressed. (c) In the first gray bar, IPTG eliminates repression of the *clts* gene by *LacI*. The cell continues to produce *Cl* when IPTG is removed. In the second gray period, the temperature is raised, eliminating repression of the *lacI* gene by *Cl* protein. Transcription of the *cl* gene stops and does not resume when the temperature is reduced. (From Hasty et al. (2002).

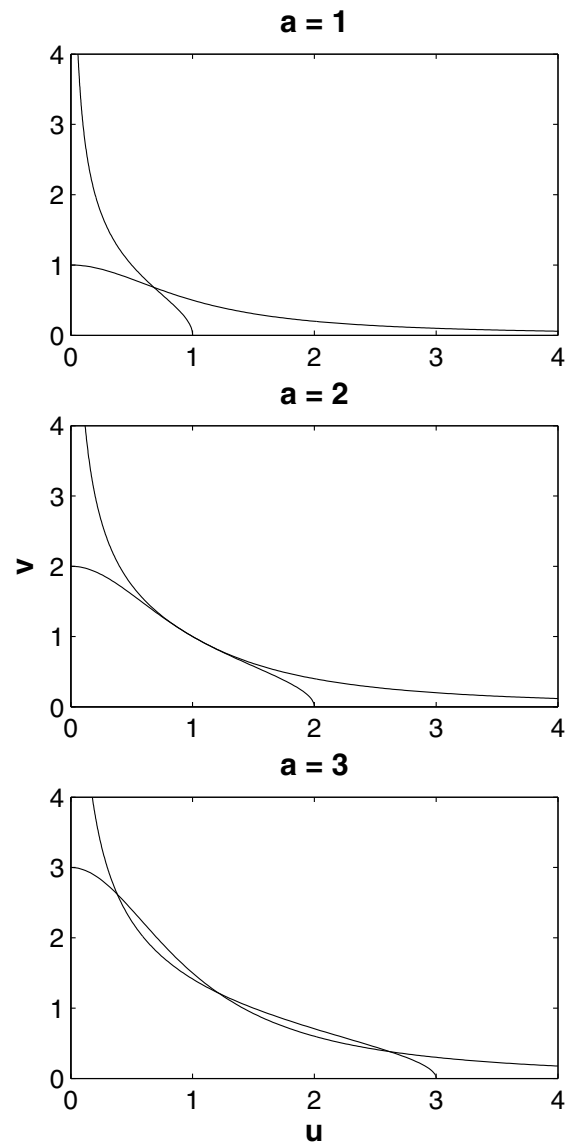


Figure 4.8: Plots of the nullclines for the toggleswitch model in the (u, v) plane for values of a below, above, and exactly at the bifurcation between 1 and 3 equilibria for the model.

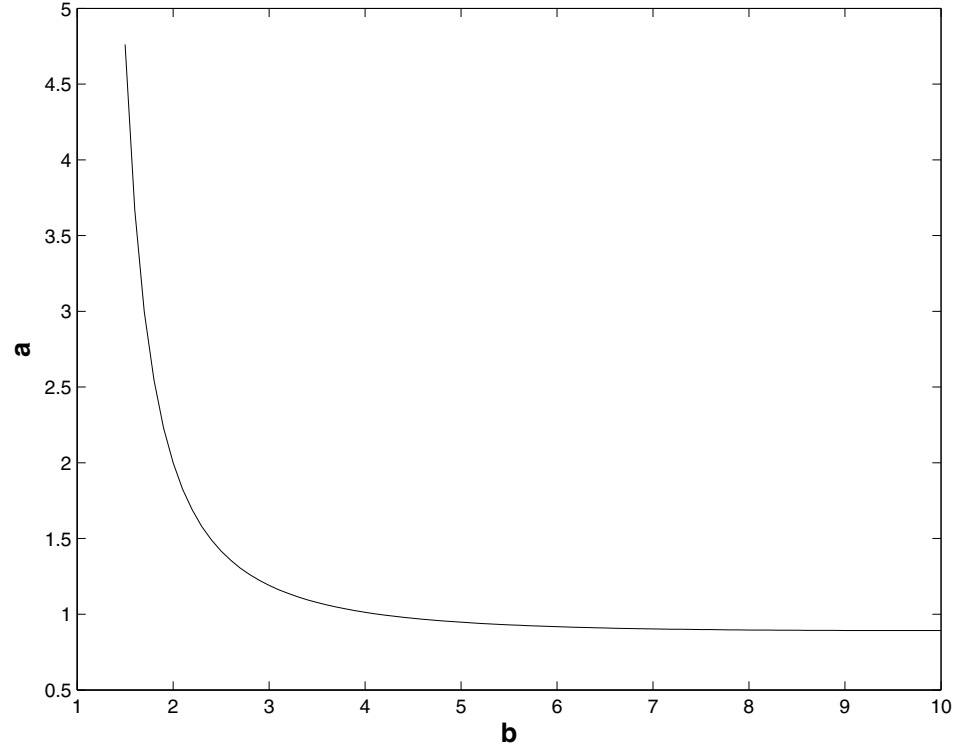


Figure 4.9: Bifurcation diagram of the $(b, a,)$ plane for the toggleswitch model. For values of (b, a) below the bifurcation curve, there is a single equilibrium point, while for values of (b, a) above the bifurcation curve, there are three equilibrium points.

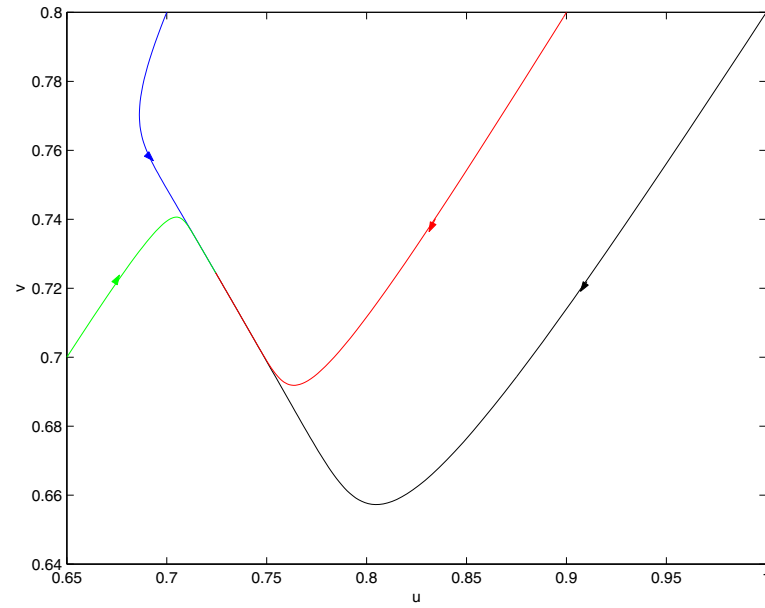


Figure 4.10: Phase portrait of the (u, v) plane for the toggleswitch model with $(b, a) = (3, 1)$. There is a single equilibrium point, which is stable and lies on the line $u = v$.

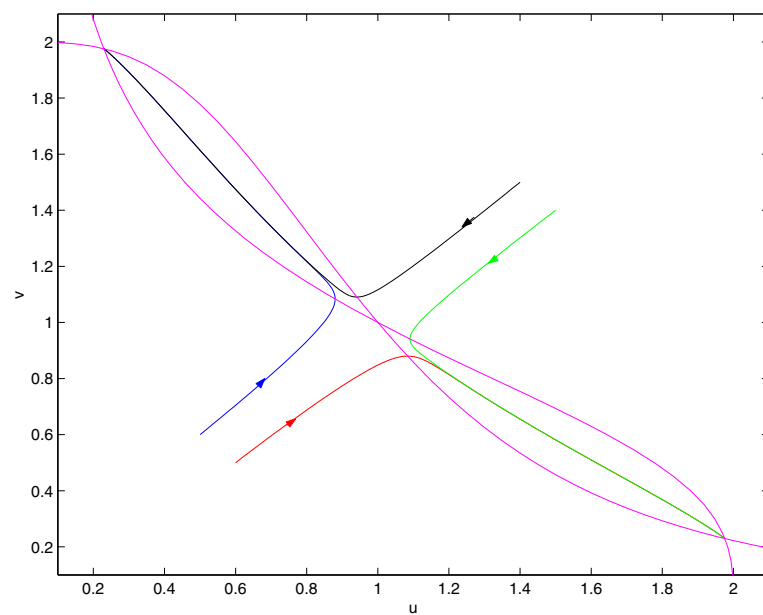


Figure 4.11: Phase portrait of the (u, v) plane for the toggleswitch model with $(e, a) = (3, 2)$. There are three equilibrium points, located at the intersections of the magenta nullclines.

5 Chapter 5

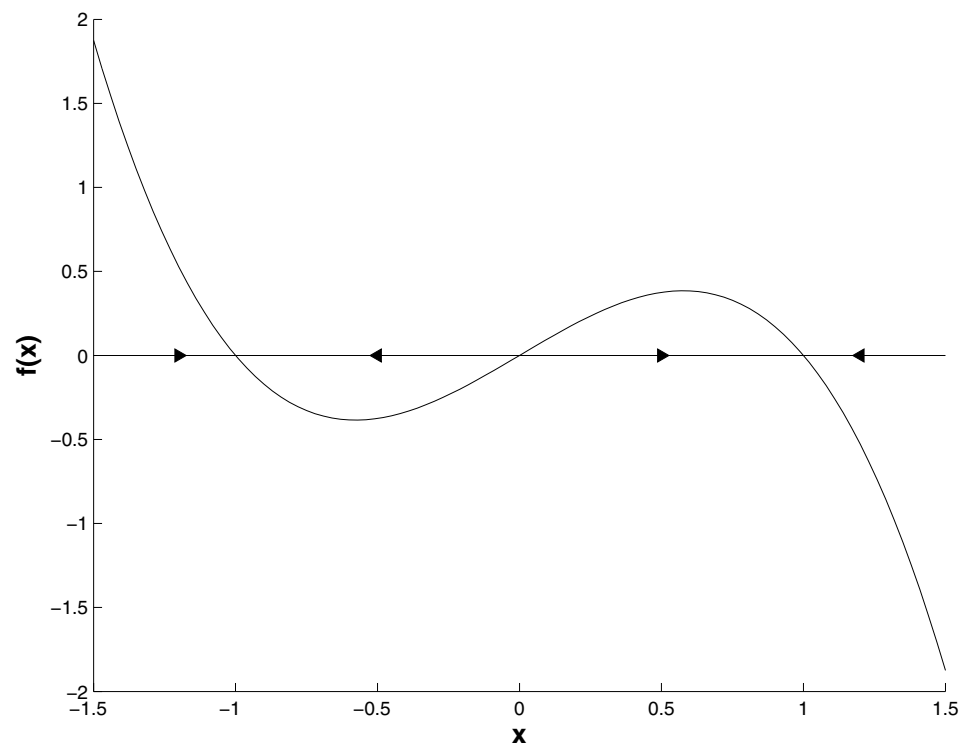


Figure 5.1: The phase line of a one dimensional differential equation with three equilibrium points. The values of the vector field are plotted as the graph of a function and arrows show the direction of the vector field along the line.

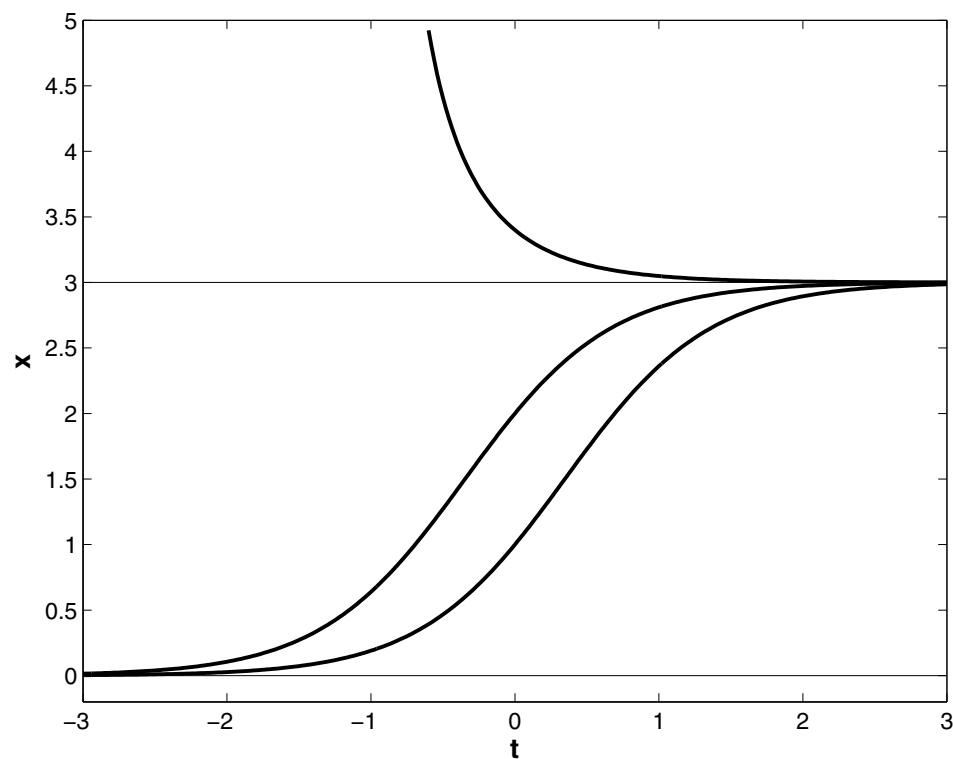


Figure 5.2: Plots of solutions $x(t)$ to the differential equation $\dot{x} = 2x(1 - \frac{x}{3})$. The equilibrium points are at $x = 0$ and $x = 3$. Solutions in the interval $(0, 3)$ approach 3 as $t \rightarrow \infty$ and 0 as $t \rightarrow -\infty$. Solutions with $x > 0$ also approach 3 as $t \rightarrow \infty$ but tend to ∞ as t decreases.

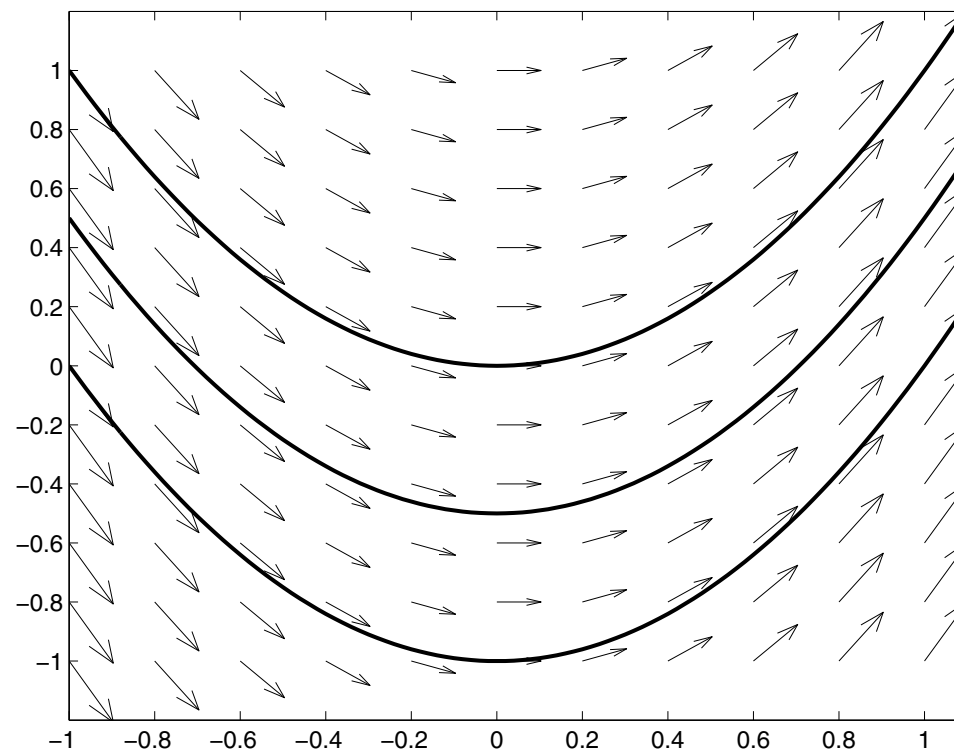


Figure 5.3: A “quiver plot” of the vector field defined by the differential equations [5.5]. The solid curves are the solutions of the equations passing through the points $(0, 0)$, $(0, -0.5)$ and $(-1, 0)$. The vector field arrows are tangent to the solution curves passing through the tail of the arrows.

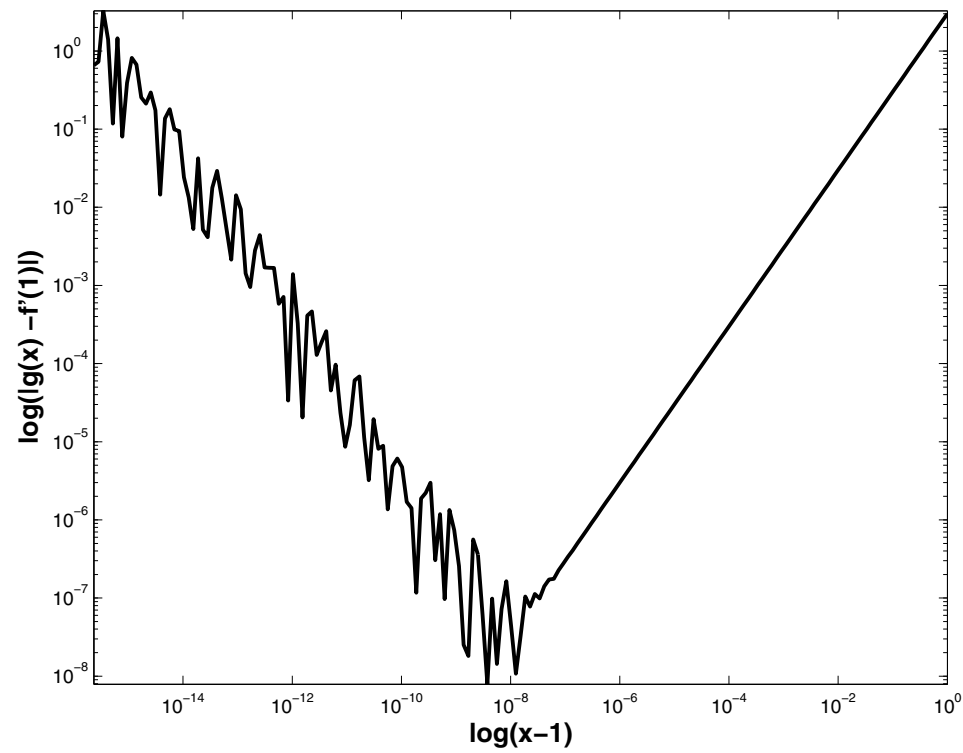


Figure 5.4: A log-log plot of the residual (error) $|r(h)|$ obtained in calculating the derivative of the function $f(x) = 1 + x + 3x^2$ with a finite difference formula.

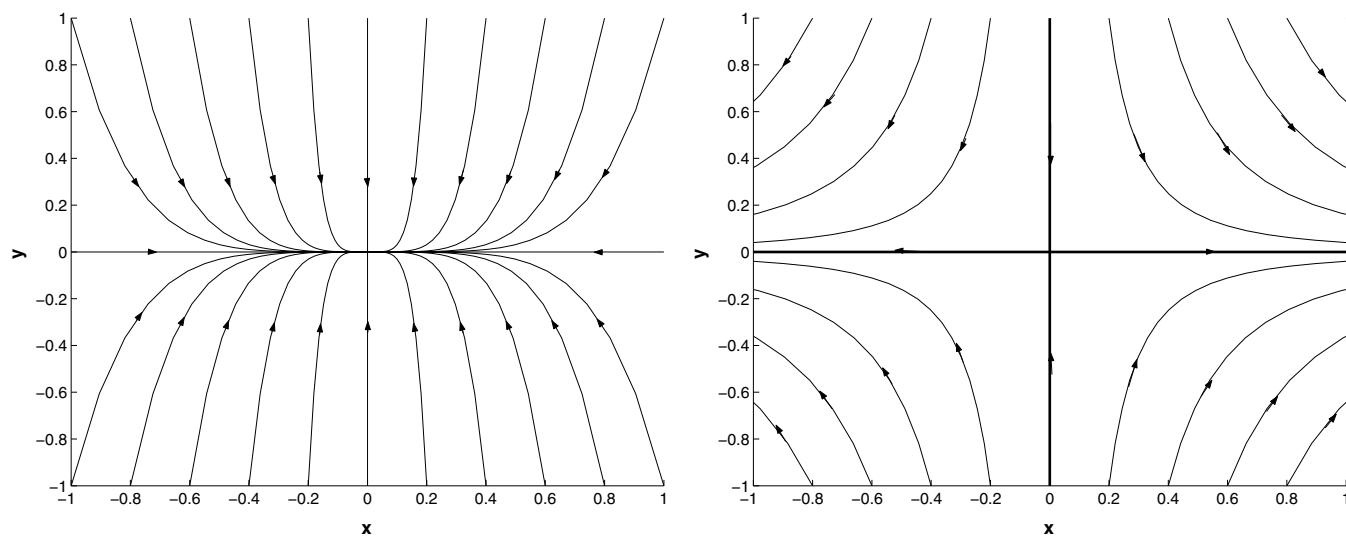


Figure 5.5: Phase portraits of two dimensional linear vector fields with (a) a stable node and (b) a saddle

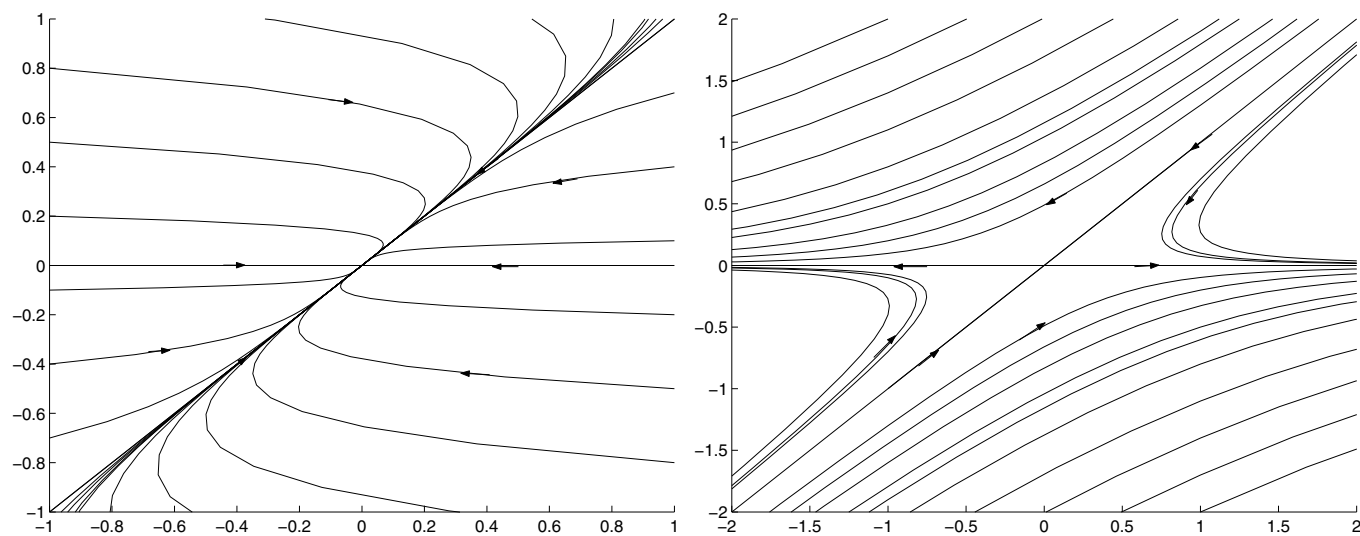


Figure 5.6: Phase portraits of two dimensional linear vector fields with (a) a stable node and (b) a saddle with eigenvectors that are not orthogonal.

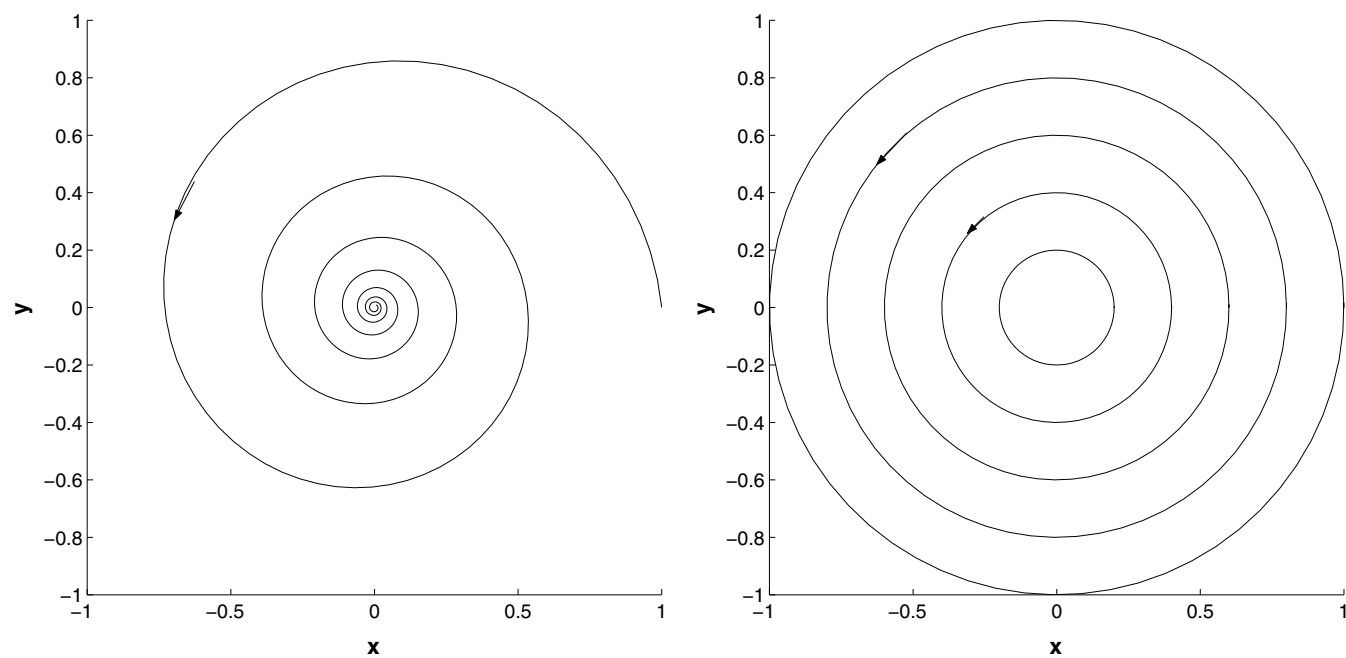


Figure 5.7: Phase portraits of two dimensional linear vector fields with (a) a stable focus and (b) a center

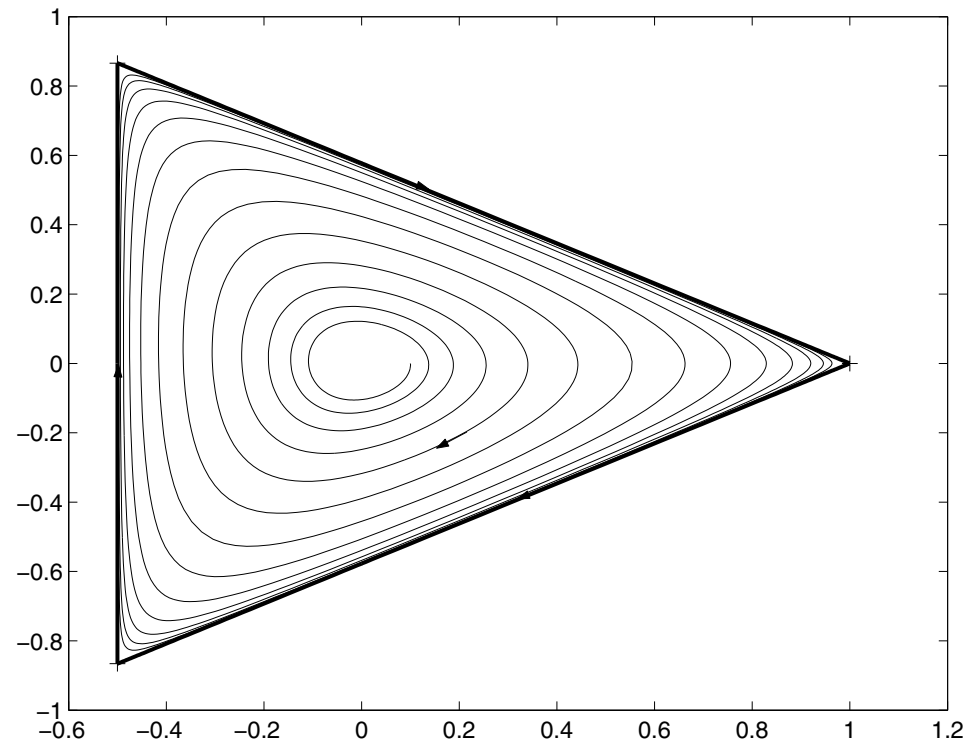


Figure 5.8: The heavy triangle is the forward limit set of the spiraling trajectory. There are three saddles at the vertices of the triangle. Each side of the triangle is a *heteroclinic* trajectory that lies in the stable manifold of one vertex and the unstable manifold of another.

<i>Parameter</i>	<i>Set 1</i>	<i>Set 2</i>
g_{Ca}	4.4	5.5
g_K	8	8
g_L	2	2
v_{Ca}	120	120
v_K	-84	-84
v_L	-60	-60
C	20	20
ϕ	0.04	0.22
i	90	90
v_1	-1.2	-1.2
v_2	18	18
v_3	2	2
v_4	30	30

Table 4: Parameter values for the Morris-Lecar system

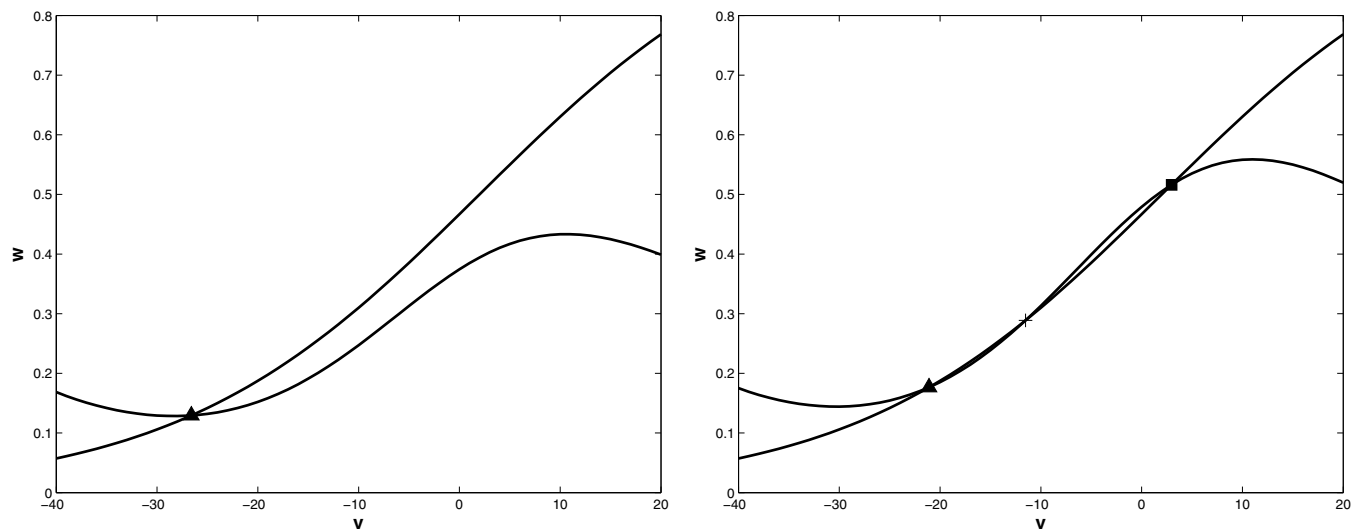


Figure 5.9: Nullclines for the Morris-Lecar model for parameter values given in Table 4

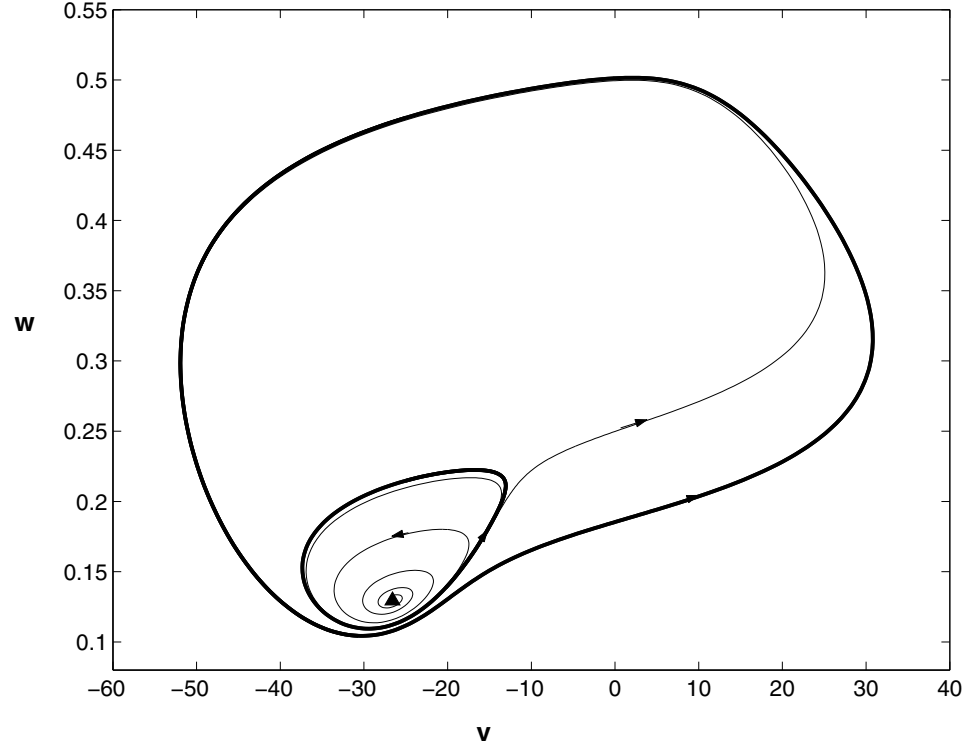


Figure 5.10: Phase portrait of the Morris-Lecar model. There are two periodic orbits (bold curves) and a stable equilibrium (triangle). One trajectory flows from the small unstable periodic orbit to the large stable periodic orbit; the remaining trajectory flows from the small unstable periodic orbit to the equilibrium point. Parameter values are given by Set 1 in Table 4

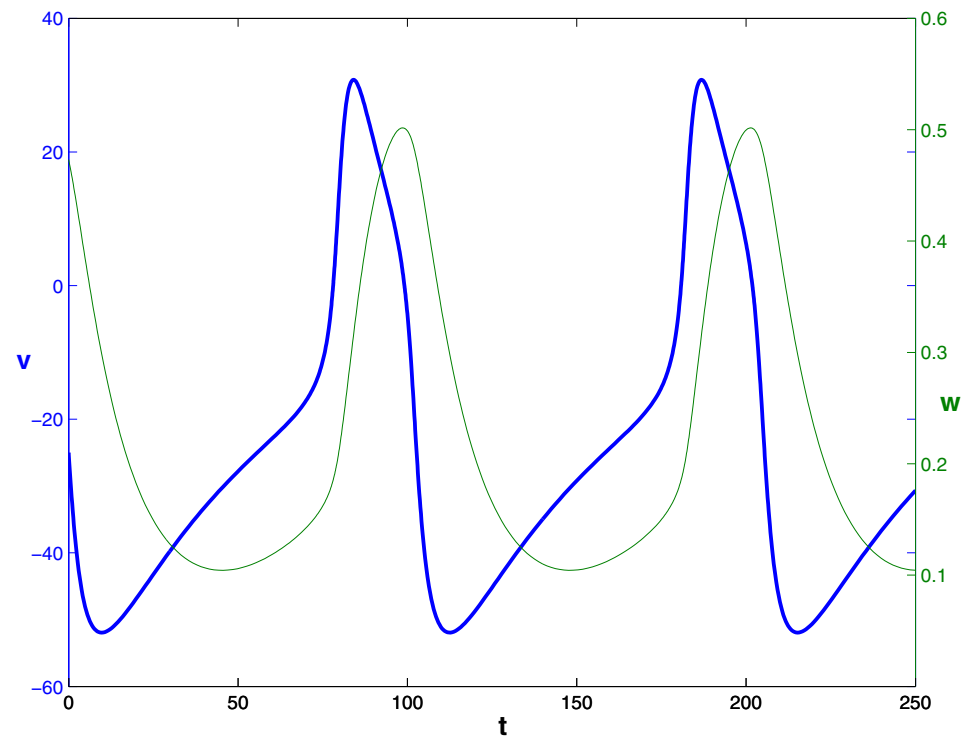


Figure 5.11: Time series of (v, w) for the large periodic orbit of the Morris-Lecar model shown in Figure 5.10. The graph of v is drawn bold.

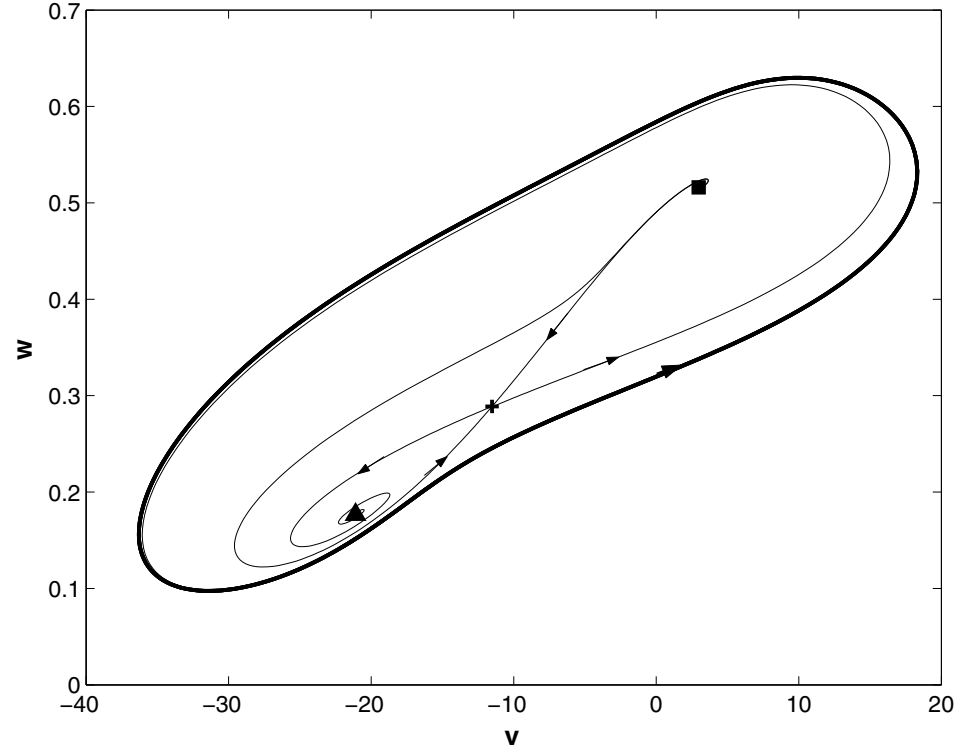


Figure 5.12: Phase portrait of the Morris-Lecar model. There is one periodic orbits (bold curve) and a three equilibrium points, one stable (triangle), one saddle (plus) and one source (square). The stable and unstable manifolds of the saddle are shown. Parameter values are given by Set 2 in Table 4

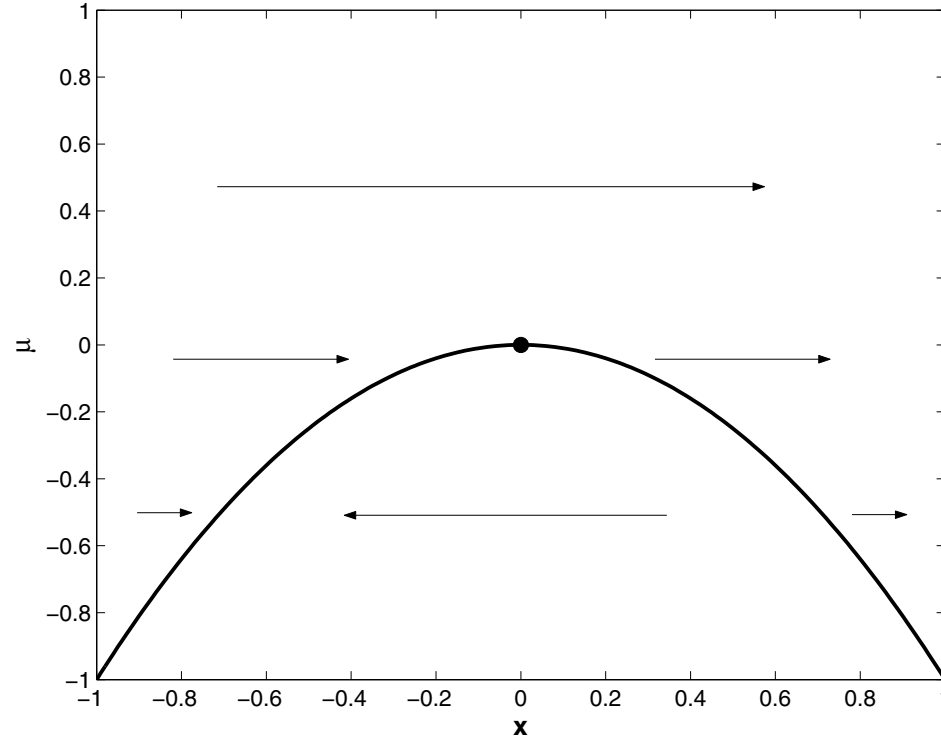


Figure 5.13: The dynamics of system (??) along the x -axis for varying μ . The equilibrium points are the parabola, with the saddle-node point at the origin. The trajectories are horizontal, with their directions shown by the arrows. Above the equilibrium curve trajectories flow right, while below the equilibrium curve trajectories flow left.

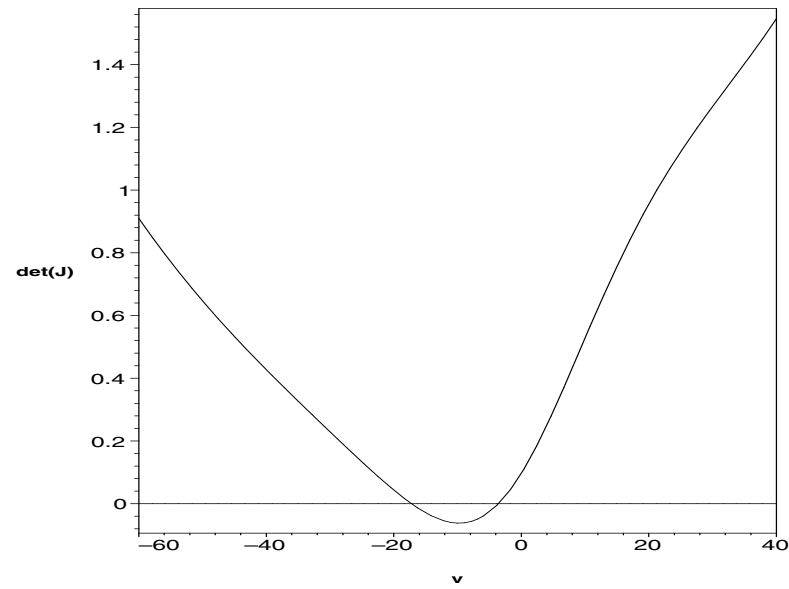


Figure 5.14: The values of w and g_{Ca} have been determined when there is an equilibrium point at a specified value of v . The determinant of the Jacobian at the equilibrium is plotted as a function of v . Saddle-node bifurcations occur when this function vanishes.

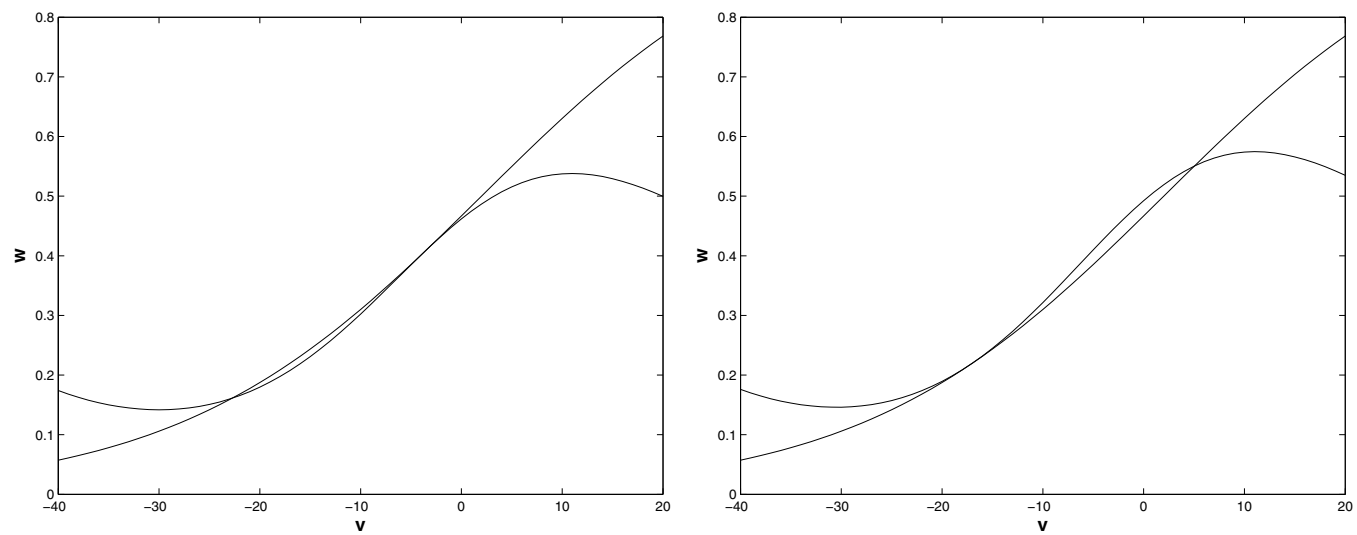


Figure 5.15: Nullclines for the Morris-Lecar system for saddle-node parameter values

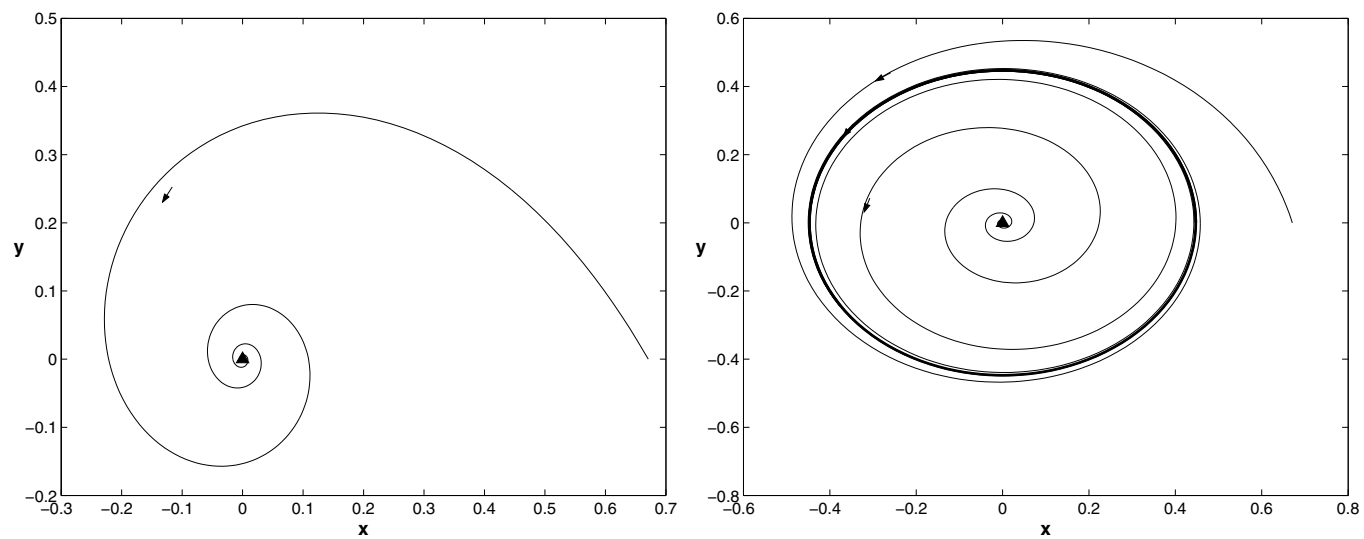


Figure 5.16: Phase portraits of the supercritical Hopf bifurcation for (a) $\mu = -0.1$ and (b) $\mu = 0.2$.

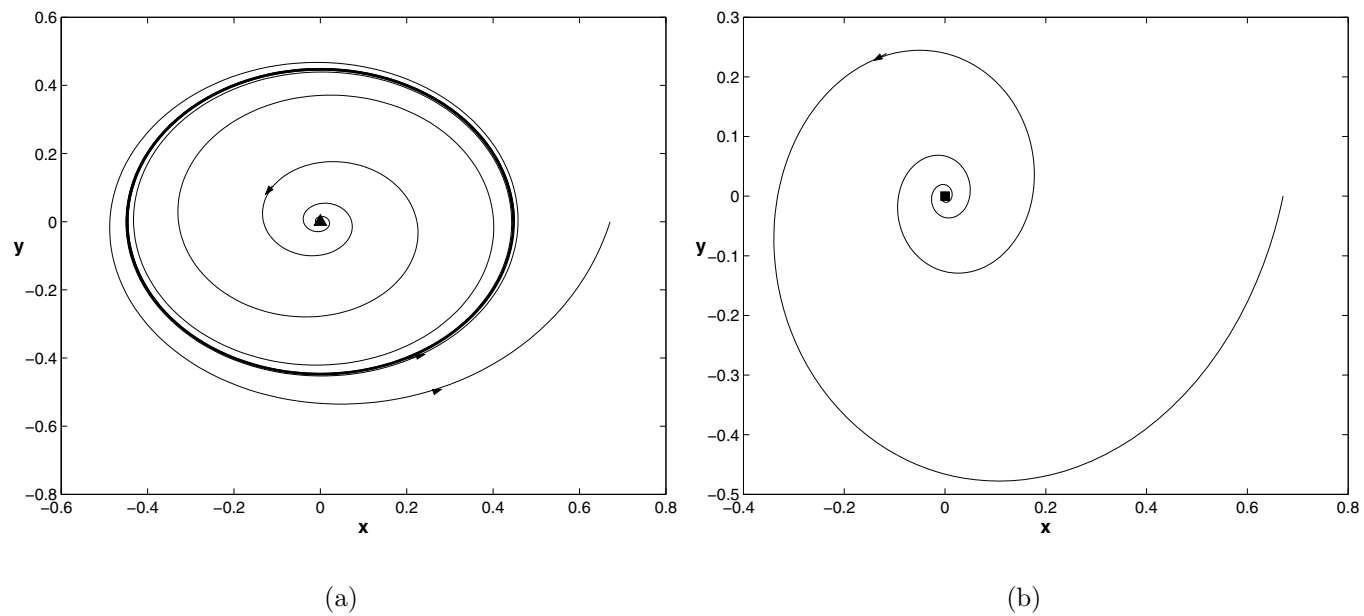


Figure 5.17: Phase portraits of the subcritical Hopf bifurcation for (a) $\mu = -0.2$ and (b) $\mu = 0.1$.

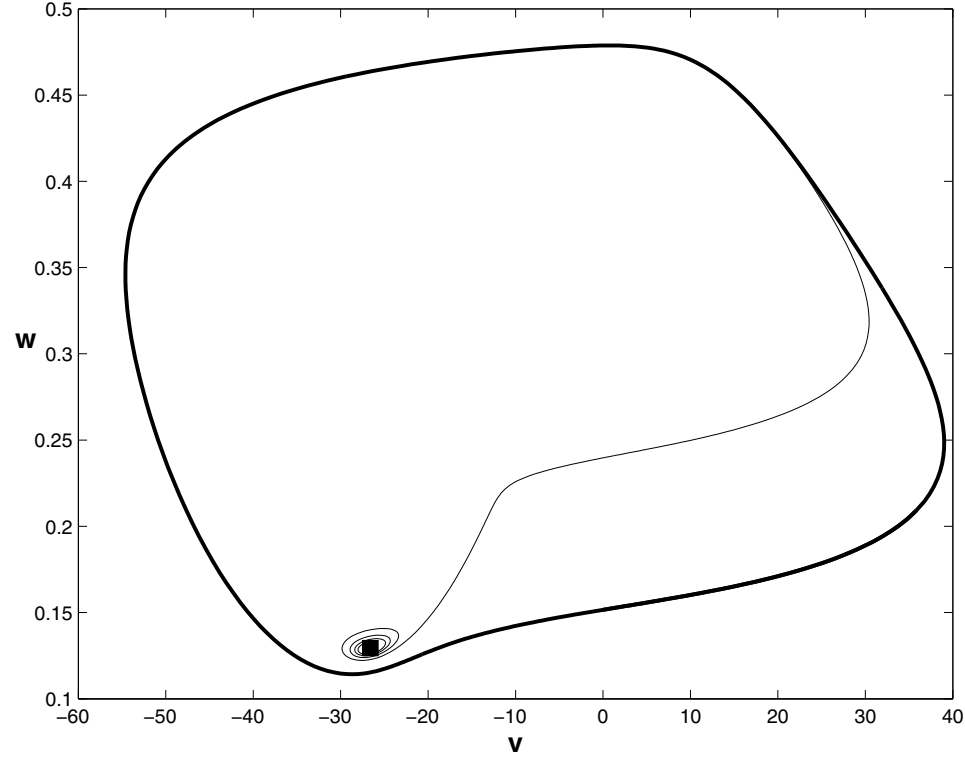


Figure 5.18: Phase portrait of the Morris-Lecar model. There is a single periodic orbit (bold curve) and an unstable equilibrium (square). Trajectories inside the periodic orbit flow from the equilibrium to the periodic orbit. Parameter values are $v_1 = -1.2, v_2 = 18, v_3 = 2, v_4 = 30, g_{Ca} = 4.4, g_K = 8, g_L = 2, v_K = -84, v_L = -60, v_{Ca} = 120, C = 20, \phi = 0.02$ and $i = 90$.

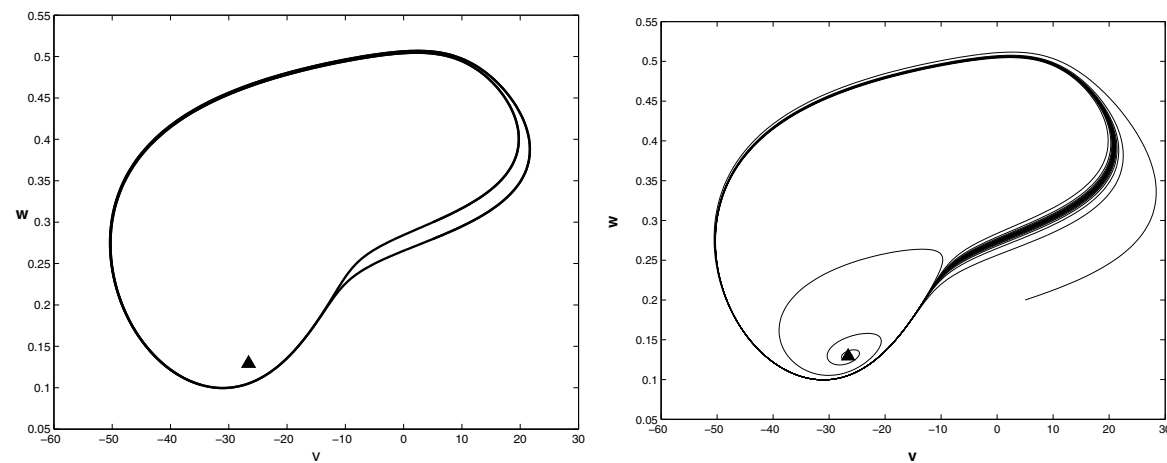


Figure 5.19: Phase portraits of the Morris-Lecar system close to a saddle-node of periodic orbits. (a) Here $\phi = 0.05201$ and there are two nearby periodic orbits. (b) Here $\phi = 0.05202$ and a single trajectory is plotted. It passes very slowly through the region where the periodic orbits were located.

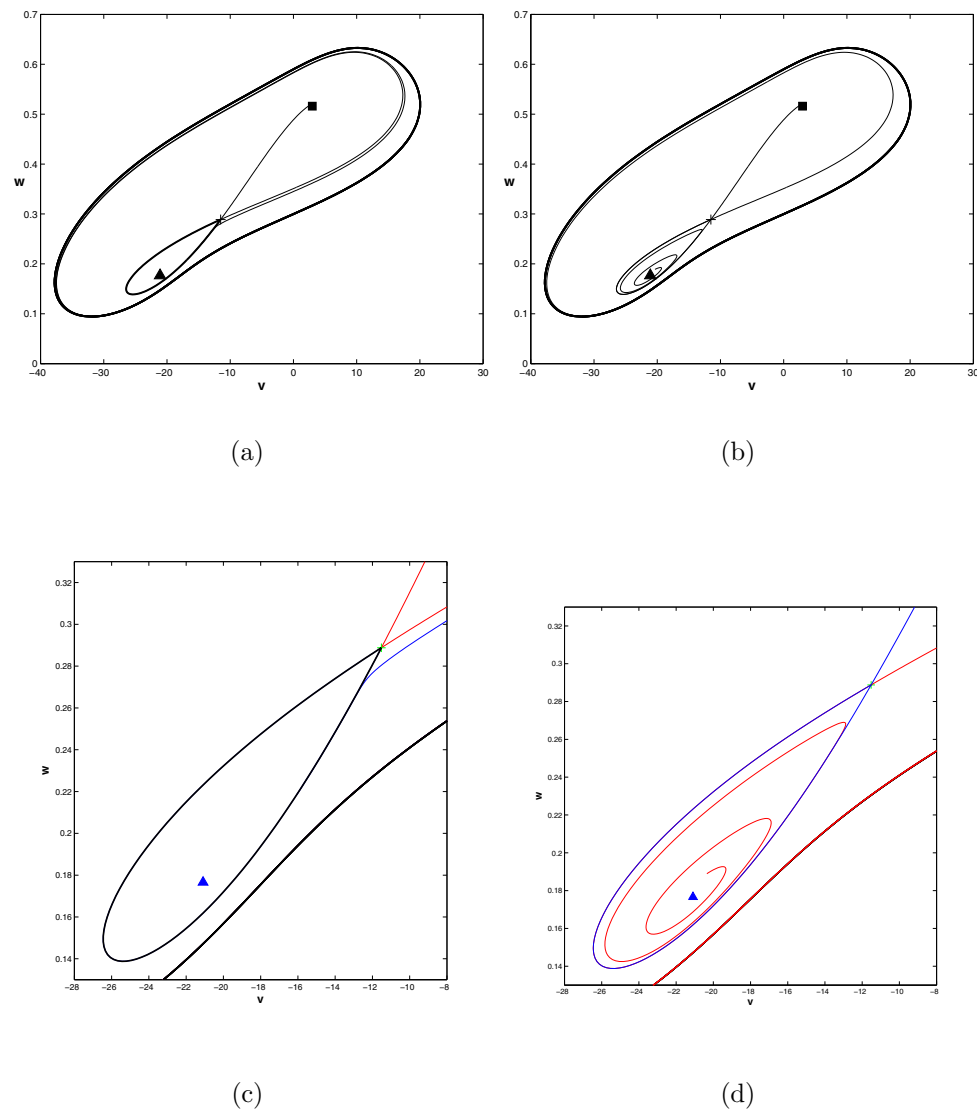


Figure 5.20: Phase portraits of the Morris-Lecar system close to a homoclinic orbit. (a) and (c) $\phi = 0.202553$ (b) and (d) $\phi = 0.202554$. The lower figures (c) and (d) show an expanded view of the upper figures (a) and (b). Observe carefully the relative position of the stable and unstable manifolds of the saddle in (c) and (d).

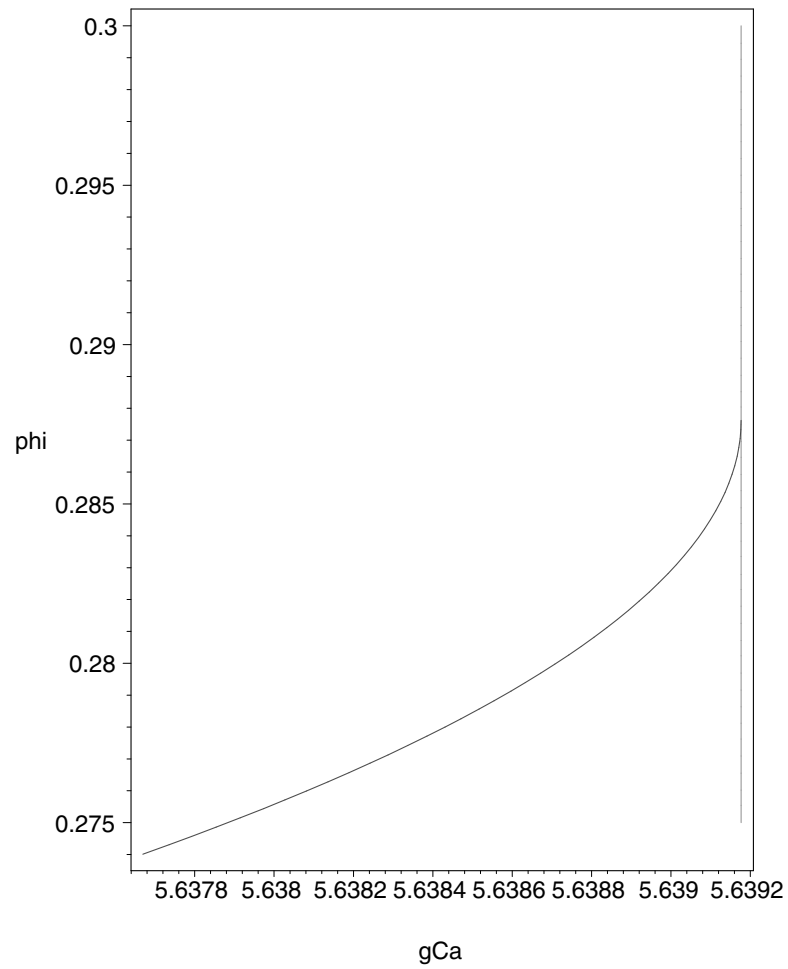


Figure 5.21: Bifurcation curves of saddle-node (vertical) and Hopf bifurcation (curved) in the plane of the parameters (g_{Ca}, ϕ) . The curves intersect tangentially at the end point of the Hopf bifurcation curve, a Takens-Bogdanov point.

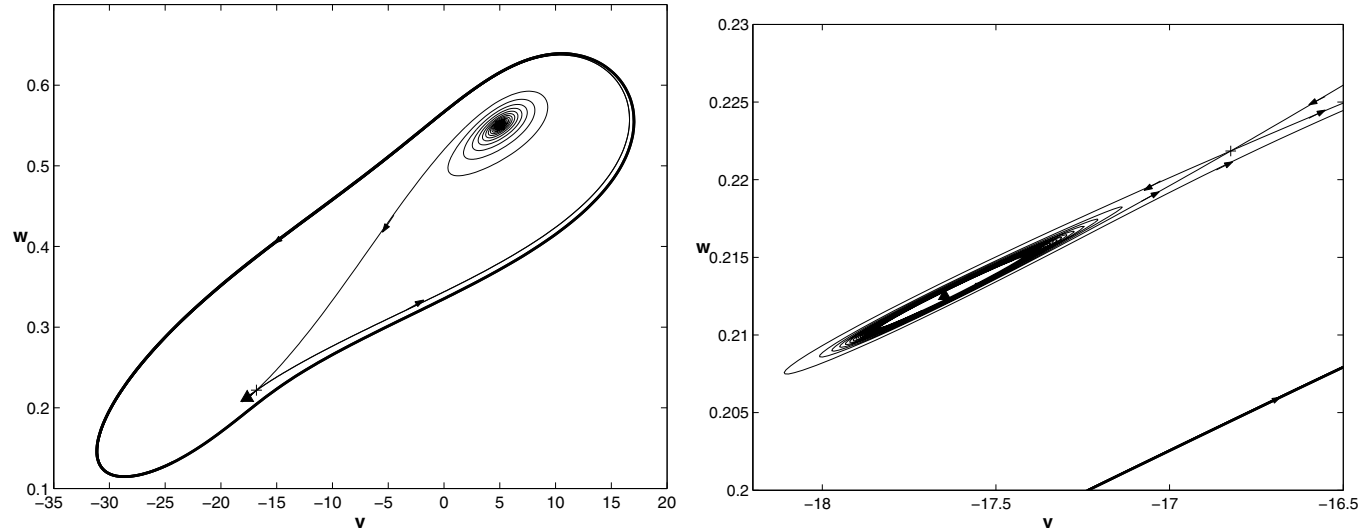


Figure 5.22: Phase portraits of the Morris-Lecar system close to a Takens-Bogdanov codimension 2 bifurcation. (a) There are three equilibrium points (a stable focus, a saddle and an unstable focus) and two periodic orbits. The small periodic orbit is not visible here, but can be seen in the small scale plot (b) of the phase portrait near the two lower equilibrium points.

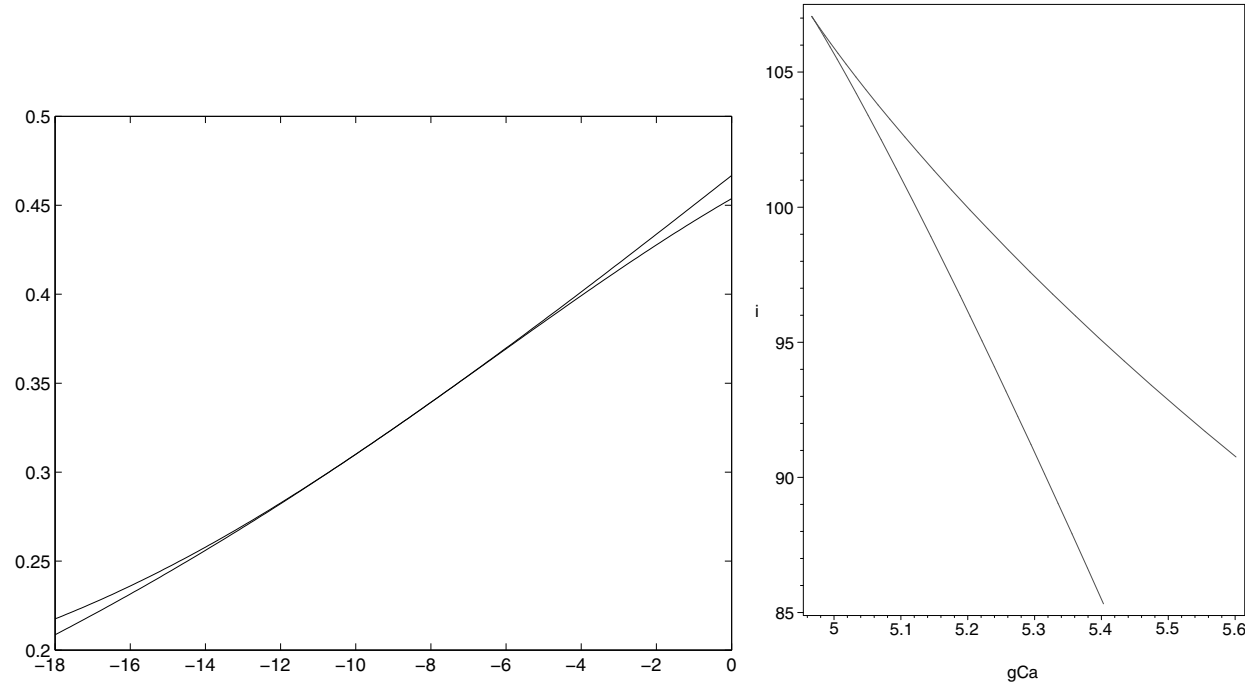


Figure 5.23: (a) Nullclines of the Morris-Lecar system at a cusp point. The two nullclines intersect at a single point to third order. The parameters are as in Table 4 except that $(g_{Ca}, i) = (4.9666, 107.06655)$. The location of the cusp point is independent of the parameter ϕ . (b) The saddle-node curve in the (g_{Ca}, i) parameter plane. The cusp bifurcation parameters are at the cusp of the saddle-node curve in this parameter plane.